

TOPICAL REVIEW

Recent developments in micromilling using focused ion beam technology

Ampere A Tseng

Department of Mechanical and Aerospace Engineering, Center for Solid State Electronics Research, Arizona State University, Tempe, Arizona 85287-6106, USA

E-mail: ampere.tseng@asu.edu

Received 10 June 2003

Published 19 January 2004

Online at stacks.iop.org/JMM/14/R15 (DOI: 10.1088/0960-1317/14/4/R01)

Abstract

The application of focused ion beam (FIB) technology in microfabrication has become increasingly popular. Its use in microfabrication has advantages over contemporary photolithography or other micromachining technologies, such as small feature resolution, the ability to process without masks and being accommodating for a variety of materials and geometries. An overview of the recent development in FIB microfabrication technology is given. The emphasis will be on direct milling, or maskless techniques, and this can distinguish the FIB technology from the contemporary photolithography process and provide a vital alternative to it. After an introduction to the technology and its FIB principles, the recent developments in using milling techniques for making various high-quality devices and high-precision components at the micrometer scale are examined and discussed. Finally, conclusions are presented to summarize the reviewed work and to suggest the areas for improving the FIB milling technology and for future research.

(Some figures in this article are in colour only in the electronic version)

1. Introduction

Miniaturization is the central theme in modern fabrication technology. Many of the components used in modern products are becoming smaller and smaller. Here, the recent development of the focused ion beam (FIB) direct milling technique will be reviewed with the focus on fabricating devices at the micrometer level. Because of the very short wavelength and very large energy density, the FIB has the ability for direct fabrication of structures that have feature sizes at or below 1 μm . As a result, the FIB has recently become a popular candidate in making high-quality microdevices or high-precision microstructures.

The FIB has been a powerful tool in the semiconductor industry mainly for mask repairing, device modification, failure analysis and integrated circuit debugging. Two basic working modes, ion beam direct write and ion beam projection, have been developed for these applications. The ion beam direct write process, also known as FIB milling (FIBM), is

the process of transferring patterns by direct impingement of the ion beam on the substrate. It is a large collection of microfabrication techniques that removes materials from a substrate and has been successfully used for fabricating various three-dimensional (3D) microstructures and devices from a wide range of materials. For the ion beam projection process, a collimated beam of ions passes through a stencil mask and the reduced image of the mask is projected onto the substrate underneath. The ion beam projection process is also known as focused ion beam lithography (FIBL) and can serve as an alternative to conventional optical lithography. However, the ion optics still remains as a major challenge since an entire image has to be projected with minimum distortion and focused over the entire field at the same time. Moreover, the new development and the latest applications of the ion beam projection technology have been thoroughly reviewed recently (Melingailis *et al* 1998, Kaesmaier and Loschner 2000). Thus, in this review, only the milling technology will be examined.

The key to the FIB direct write or milling technology is its ability to operate a FIB with a proper beam size, shape, current and energy to remove a required amount of material from a pre-defined location in a controllable manner. In this way, high-precision and complex 3D structures can be sculpted. However, when an energetic ion hits the surface of the target, a variety of ion–target interactions, including swelling, deposition, milling, implantation, backscattering and nuclear reaction, can occur (Brodie and Muray 1992). The most important interaction for milling is that the energy transferred from the ions to the target substrate is high enough, leading to a collision cascade involving substrate atoms at or near the surface where sputtering and redeposition are the two governing effects that cause material removals. For the majority of the ion sources used in the FIB, the optimized ion energy leading to surface collision cascade of most engineering target materials is in the range of 10–100 keV. For ion energy higher than 100 keV, implantation occurs as the ions can easily penetrate into and be trapped in the interior of the substrate, while for ion energy higher than 1 MeV, backscattering and nuclear reaction become dominant. Here, only the major effects for controlling the milling behavior (sputtering and redeposition) will be reviewed.

In this review, after an introduction to the FIB technology and its principles, the recent developments on using the milling techniques for making various high-quality microdevices or high-precision microcomponents for optical, magnetic, electronic, electric, mechanical, thermofluidic, biochemical and biomedical applications are reviewed and discussed. The basic phenomena of sputtering yield will be examined first. The effects of ion species, incidence angle, ion energy and ion interaction with the target materials will be quantitatively studied by comparing the published experimental data with the numerical results to provide the basis or guidance for appropriate selections of these operating parameters necessary for high-precision milling processes. The redeposition effect is evaluated by studying the profiles made by single-pass milling, which is a basic milling mode. The profiles milled by repetitive (multiple) passes are then assessed. The influences of the scanning strategy or sequence on the milled geometries are also included in the assessment. The procedures used to mill different microcomponents and devices for mechanical, electronic, optical and magnetic applications are presented to illustrate the versatility and advances of the FIB techniques. Finally, conclusions that summarize the review findings and suggest the area for future work are included.

2. FIB technology

The ion beam has many advantages over other high-energy particle beams. For example, as compared to photons or electrons (e^-), ions are much heavier and can strike with much greater energy density on the target to directly write or mill patterns on hard materials, such as semiconductor, metal or ceramic substrates. On the other hand, photons and electrons can only effectively write on or expose soft materials, such as photoresists or e-beam resists. The resists are normally used as the media to transfer the patterns to silicon or other substrates in the procedures normally used in the photolithographic or e-beam lithographic process. Therefore,

the direct writing capability of the FIB can reduce various hassles and defects caused by the masks and resists in pattern transfer. Also, as compared with e-beams, the FIB does not generate high-energy backscattered electrons, which often limits the minimum linewidth attainable by the e-beam lithographic or lift-off process (Tseng *et al* 2003). On the other hand, because ions are much heavier, the lateral scattering of the FIB is relatively low, resulting in striking only the intended regions. Thus, a fine FIB beam can directly write a very narrow line.

2.1. Ion sources

With the recent advent of powerful sources such as the liquid metal ion source (LMIS) in the late 1970s as well as the advances in ion optics in the late 1980s, FIB technology has been developing rapidly and so have its applications (Orloff 1993, DeJager and Vijgen 1994, Reyntjens and Puers 2001). The range of materials being used in FIB systems is also expanding to further increase the extent of their applications. The ion sources that are currently available include Al, As, Au, B, Be, Bi, Cs, Cu, Ga, Ge, Er, Fe, H, In, Li, Ni, P, Pb, Pd, Pr, Pt, Si, Sn, U and Zn. Many of these ion species are produced from liquid-metal alloy sources because of the high melting temperature and the reactivity or volatility associated with the pure metal species. Ar, B and P ions are particularly interesting because of their use in implantation of semiconductor materials. The popular ion species for microfabrication are As, Be, Ga and Si.

2.2. Ion–target interaction

An energetic ion can interact with a target surface in various ways. Depending on the ion energy, the interaction can be swelling, deposition, sputtering, redeposition, implantation, backscattering or nuclear reaction. However, some of the interactions are not completely separable and may lead to unwanted side effects that need to be understood and avoided for a specific application. For milling applications, it is desirable that the incoming ions interact only with the atoms at the surface or near the surface layer of the target substrate and also lead to a collision cascade on the atoms. If the ion energy (or momentum) is adequate, the collision can transfer sufficient energy to the surface atom to overcome its surface binding energy (3.8 eV for Au and 4.7 for Si), and the atom is ejected as a result. This interaction is called sputtering and is the governing effect in FIB milling. Because the interaction depends solely on momentum transfer to remove the atoms, sputtering is a purely physical process.

The sputtering yield, defined as the number of atoms ejected per incident ion, is a measure of the efficiency of material removal. The yield is normally in the range of 1–50 atoms per ion and is a function of many variables, including masses of ions and target atoms, ion energy, direction of incidence to the surface of the target, target temperature and ion flux. Initially, the sputtering yield increases as the ion energy increases, but the yield starts to decrease as the energy is increased past the level where the ions can penetrate deep into the substrate. At this stage of interactions, implantation or doping can take place in which the ions become trapped in the substrate as their energy is expended (Brodie and Muray

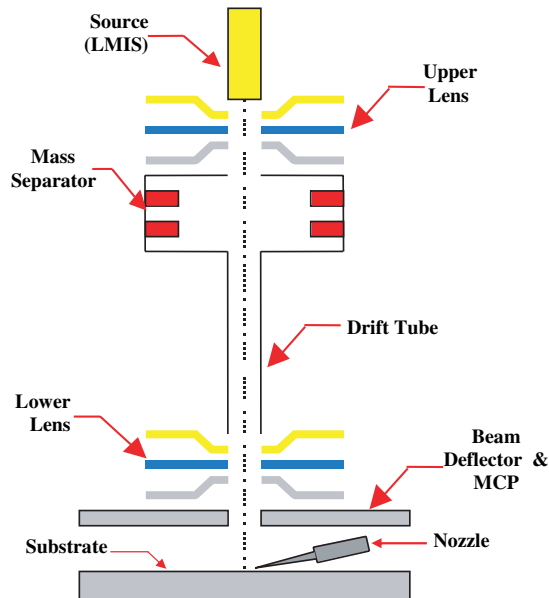


Figure 1. Schematic diagram of a two-lens FIB system.

1992). As a result, the proper energy for sputtering is between 10 and 100 keV for most of the ion species used for milling.

During sputtering, a portion of the ejected atoms or molecules is frequently redeposited into the sputtered region and this redeposition makes it difficult to control the amount of material removed by sputtering. In fact, the essence of FIB milling is to carefully control both the material sputtering and the redeposition, so that a precise amount of material can be removed. It should also be noted that since the FIB implantation is mainly material property alteration in nature instead of material removal, only sputtering and redeposition will be examined in this review. Furthermore, to have a more focused review, other related FIB techniques, including chemical enhanced effects for either etching or deposition, will not be included.

2.3. FIB systems

The basic components of a FIB system are normally an ion source, an ion optics column, a beam deflector and a substrate stage. Figure 1 schematically shows a FIB system with a two-lens (or twin-lens) column (Wang 1997). The LMIS has been widely used to provide reliable and steady ion beams for a variety of ion species. A LMIS typically consists of a capillary tube with a needle through it, an extraction electrode, and a shielding, as shown in figure 2. The capillary acts as a reservoir that feeds liquid metal to the tip. The interaction of the strong electric–static force generated by the extraction electrode and the surface tension causes the liquid metal meniscus to form a sharply peaked cone, also known as the Taylor cone (Brodie and Muray 1992). The application of the critical Taylor voltage on the liquid metal cone extracts positively charged ions. The ions are collimated into parallel beams by the upper (condenser) lens.

Then the ion beam is passed through a mass separator and a drift tube. A mass separator is set up to allow only the required amount of ions with a fixed mass–charge ratio to

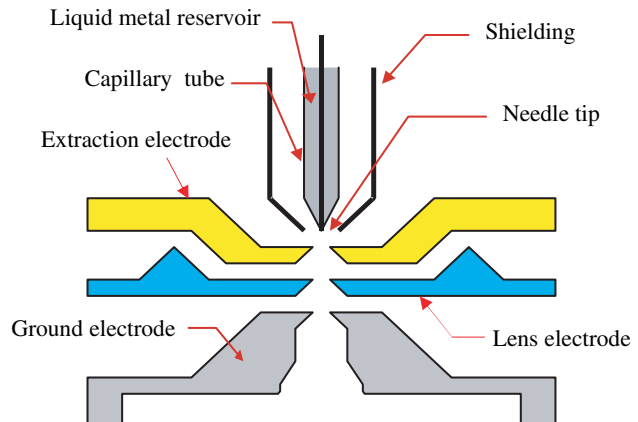


Figure 2. LMIS in a two-lens system.

pass through (Ward 1985). Below the mass separator there is a long and thin drift tube, which eliminates the ions that are not directed vertically. The lower (objective) lens is located below the drift tube and it helps in reducing the spot size of the ion beam and in improving the focus. Following the objective lens is an electrostatic beam deflector, which controls the final trajectory or landing location of the ions on the substrate. The nozzle shown in figure 1 can be used for FIB-induced etching or chemical vapor deposition, which are subjects that are beyond the scope of this review and will not be discussed further.

Often, a multi-channel plate (MCP) is located above the target. The MCP helps in recording the secondary electron emission and thereby helps in viewing the substrate (Reyntjens and Puers 2001). The whole setup is usually placed in a low-pressure chamber evacuated to the 10^{-7} Torr regime. This is done so that the mean free paths of the ions are increased and the strength of the beam is not reduced due to the interference of the particles in the chamber (Melingailis 1987, 2001). This system usually produces ion energies from 50 to 250 keV with the minimum full width at half-maximum (FWHM) beam diameter down to 50 nm and it can be used for both sputtering and implantation (Harriott 1991, Bi *et al* 1998). Many alloys can be used in this type of system to produce different types of ion sources (Takai *et al* 1996). The FWHM is commonly used to describe the diameter of a FIB, in which the ion intensity is highly non-uniformly distributed; frequently, its intensity is close to a Gaussian profile. The FWHM is defined as the distance between the locations on the intensity profile at which the intensity reaches half of its maximum value.

FIB systems with a single-lens column have also been used for providing relatively low-energy ions at the range of 10–50 keV (Harriott 1991, Yu *et al* 1994). In a single-lens system, the ions are extracted from the LMIS and passed through a beam-limiting aperture to an electrostatic lens. The single-lens FIB system does not have the lower lens as those in the two-lens system (figure 1), but it uses the limiting aperture for controlling the ultimate beam size. Typically, the limiting aperture can be adjusted from tens to hundreds of micrometers in diameter and is located between the extraction electrode and lens electrodes, as shown in figure 2. The lens electrodes in the single-lens system are used for focusing the ion beam

and reducing its size, so that the beam diameter can be much smaller than the aperture diameter.

Similar to the two-lens system, the single-lens system has a beam deflector located above the target. In microfabrication, a heavy ion species, such as gallium ions, is usually used in this low-energy type of system to increase its sputtering effectiveness. In addition to its cost advantage over the two-lens system, the single-lens system with appropriate control of beam current and sizes has the capability to make a high-precision microstructure with a feature size down to 10 nm and it has been popular for microfabrication research and low quantity production. On the other hand, the two-lens system is more popular in industry and in special purpose research because of its high production rates and its ability to handle a variety of ion species for both milling and implantation. The choice of the ion species or the type of system is mainly dictated by the application and availability.

3. Ion sputtering

The ion milling process is a combination of physical sputtering and material redeposition. The relatively high-energy density and small size of the FIB enable the substrate material to be removed on a submicrometer scale. This includes substrates that cannot be structured using standard photolithography. The material removal rate by sputtering, or the sputtering yield, is dependent not only on the substrate material, but also on many processing parameters, including the ion energy, the angle of incidence and the milling conditions. Understanding these processing parameters can lead to enhancing the sputtering rate and further improving the material removal rate in milling. In this section, the sputtering yield for different substrates at different processing conditions will be studied to characterize the basic sputtering phenomena, which are essential to the milling process for making microstructures from simplified two-dimensional (2D) structures (such as microchannels and microholes) to complicated 3D structures.

A software package, TRIM (TRansport of Ions in Matter), has been widely used for predicting the sputtering yield for many different ions at a wide range of energy. TRIM is a comprehensive Monte Carlo program, which calculates the stopping range of ions (10 eV–2 GeV per atomic mass unit) into matter using a quantum mechanical treatment of ion–atom collisions (Biersack and Haggmark 1980). This calculation is made very efficient by the use of statistical algorithms, which allow the ions to make jumps between the calculated collisions and then average the collision results over the intervening gaps. It provides the distribution of the ions and the kinetic phenomena associated with the ion's energy loss, including target damage, phonon production, ionization, and ion reflection, implantation and sputtering.

Figure 3 shows TRIM simulations of 1000 As ions with 30 and 90 keV ion energies implanting vertically into a gold substrate (normal to the target surface, the incidence angle equals 0°). The left column of the figure indicates the ion trajectories in the Au substrate and the range of implanted ions is predicted from this simulation. The right column indicates the moving and stopped recoiling atoms of the target substrate. The number of recoiling atoms out of the target surface is the sputtering yield. As shown, although the region

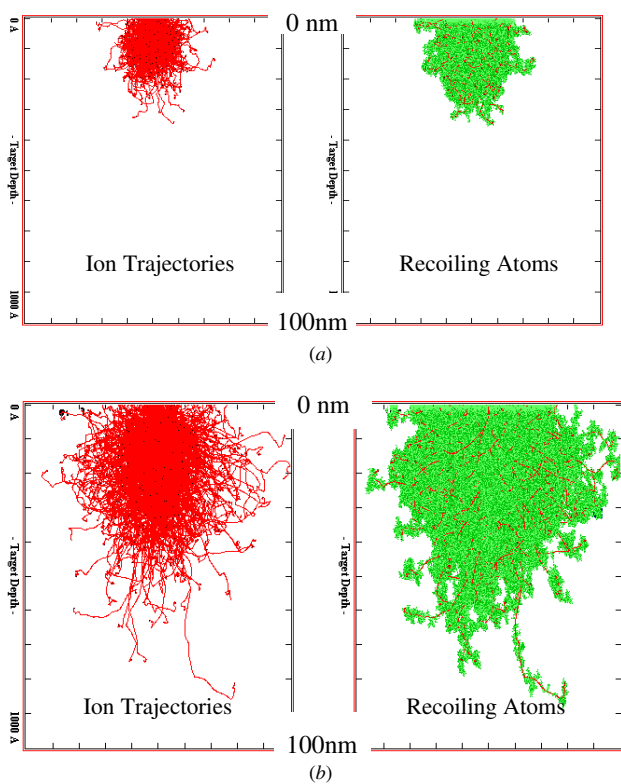


Figure 3. TRIM Monte Carlo simulation of 1000 ion sputtering: (a) 30 keV As ions into Au substrate; (b) 90 keV As ions into Au substrate.

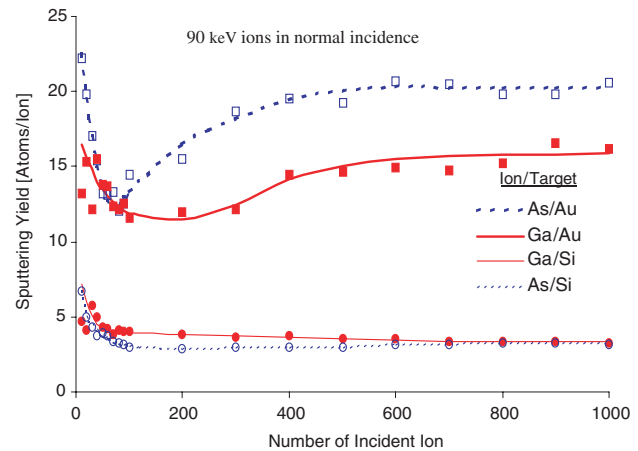


Figure 4. Effect of ion number in the TRIM simulation.

of the moving and stopped recoiling atoms is larger than that of the penetrated ions, the target depths (penetration depth for the ions or influence depth for the atoms) are similar. Both the penetration and the influence depths propagate linearly from 30 to 90 nm as the ion energy increases from 30 to 90 keV. Since TRIM is based on the Monte Carlo method, the number of ions used in the simulation can have an effect on the results. Figure 4 shows the influence of the number of ions used on the four different sputtering-yield simulations and the results indicate that the simulations become converged when the ion number surpasses 500. To be conservative, 1000 ions are used for all of the TRIM simulations presented here.

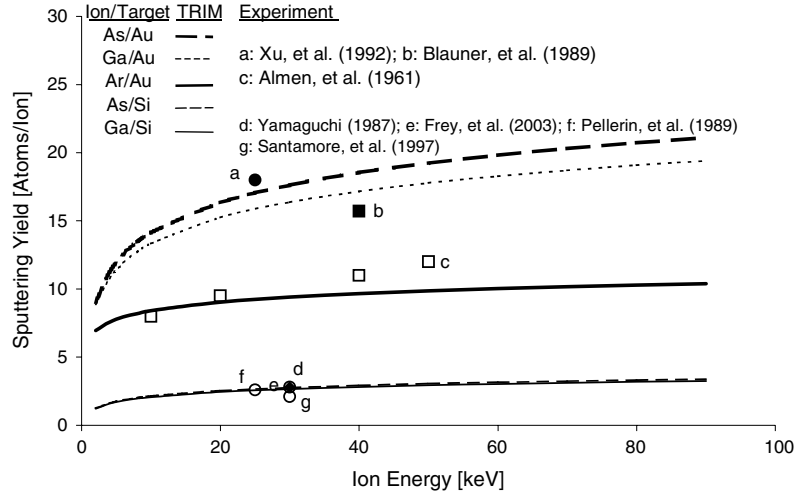


Figure 5. Energy dependence of sputtering yield of Au and Si target substrates by three types of ions at normal incidence.

The dependences of the sputtering yield on ion energy, incident angle and target material have been studied both theoretically and experimentally. Figure 5 shows the theoretical predictions of sputtering yield by TRIM for two types of target substrate (Au and Si) using three types of ion source (As, Ga and Ar) at normal incidence as a function of the ion energy. As shown, the sputtering yield grows as the ion energy increases, but its rate of increase reduces as the ion energy increases. The figure also shows that the sputtering yield of the Au substrate is much higher than that of the Si substrate and, in general, heavier ions can produce higher sputtering yields. The atomic (or ion) weights of As, Ga and Ar are 74.9, 69.7 and 39.9, respectively. Although the data are not shown, in most cases, the sputtering yield either levels off or decreases for ion energies higher than 100 keV. This confirms our earlier discussion that implantation takes place at relatively high-energy interaction, as ions penetrate into the substrate and are trapped in the lattices. The Si and Au targets considered here are the two most popular substrates used in microfabrication and nanofabrication and will be used as the example substrates for later discussion. To gage their reliability, the TRIM predictions are further compared to the experimental data reported by eight different research groups in the past 30 years (Almen and Burce 1961, Yamaguchi 1987, Blauner *et al* 1989, Pellerin *et al* 1989, Xu *et al* 1992, Santamore *et al* 1997, Lehrer *et al* 2001, Frey *et al* 2003). As shown in figure 5, the TRIM predictions agree very well with the experiments for the three cases sputtered by either Ga or Ar ions. Also, the TRIM predictions for As ions are presented here because they can be used for the comparison to the FIB milling experiments discussed later. Since the data presented by Lehrer *et al* (2001) are almost identical to those of Frey *et al* (2003), only the latter is cited in figure 5.

Figure 6 shows the TRIM simulation of the dependence of the sputtering yield on the incident angle at two different ion energies. Two types of ion, As and Ga, in sputtering of Au and Si substrates are considered. As shown in figure 6, for all of the cases considered, increasing the incidence angle increases the sputtering yield until it reaches its maximum near 80°; then it decreases very rapidly to zero as the incident angle approaches 90°. As mentioned earlier, the amount of sputtering is

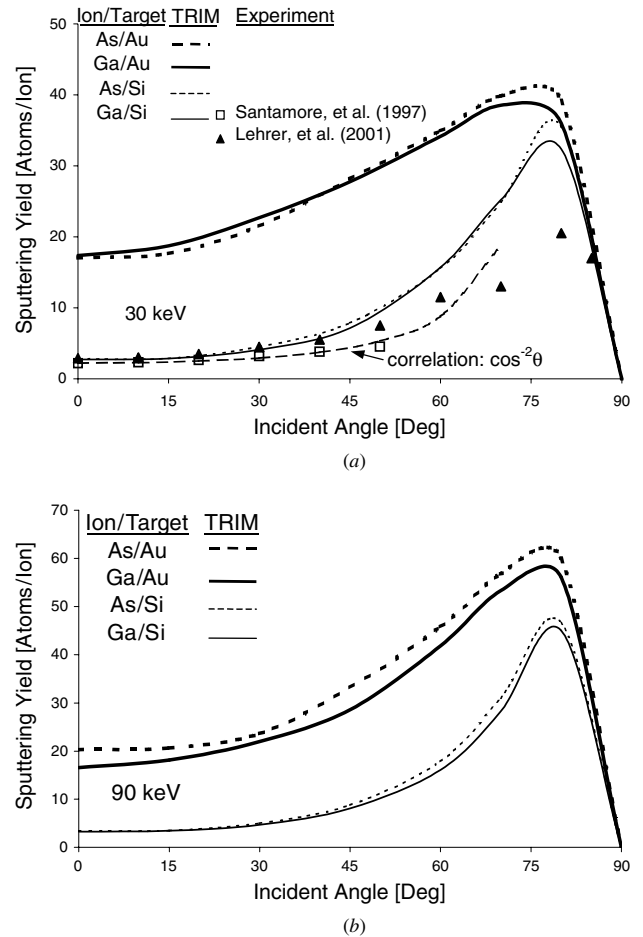


Figure 6. Angular dependence of sputtering yield of As and Ga ions on Au and Si substrates: (a) As and Ga ions at 30 keV; (b) As and Ga ions at 90 keV.

dominated by surface collision cascades. Roughly speaking, as the angle of collision between the ions and target atoms increases from normal incidence, the possibility of the target atoms escaping from the surface during the collision cascades increases and eventually this leads to an increased sputter

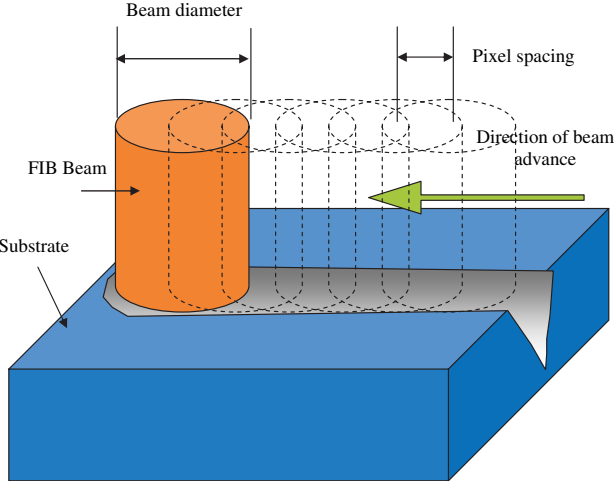


Figure 7. Schematic diagram of FIB milling.

yield. After reaching a maximum, the sputter yield decreases again as the ion approaches glancing incidence because of the increase in reflected ions and the fact that more and more collision cascades terminate at the surface before they are fully developed.

Figure 6 also shows that the sputtering yield of the Si substrate by As and Ga ions at 30 keV increases about 12 times from the normal incidence to the angle at its peak while the corresponding sputtering yield for the Au substrate increases less than 2.5 times. Moreover, when the ion energy increases from 30 to 90 keV, the peak of the sputtering yield increases approximately 10% for the Si substrate but more than 30% for the Au substrate. Figure 6 also plots the experimental results reported by Santamore *et al* (1997) and Lehrer *et al* (2001) for Ga ions/Si substrate at 30 keV and a normalized correlation of $1/\cos^2(\theta)$, where θ is the incident angle. As shown, good agreement has been found between the TRIM predictions and the experimental results, especially for incident angles less than 60° . In fact, the experimental results fall in between the TRIM predictions and the correlation. For larger incident angles, the TRIM prediction is much higher than the experimental observation. At glancing angles, surface channeling plays an important role and causes the sputtering yield to decrease. The behavior of the angular dependence of sputtering yields has been observed by many other researchers, including Yamamura *et al* (1983) and Vasile *et al* (1999).

4. Uniform ion flux for smooth milling

In a computer-controlled FIB machine, milling is performed by a precise pixel-by-pixel movement. This is also known as a digital scan and is schematically shown in figure 7. The amount of time that the beam remains on a given target pixel is called the dwell time (t_d). The distance between the centers of two adjacent pixels is called the pixel spacing (p_s).

4.1. Raster and serpentine scans

To mill a pattern on a substrate, the pattern should be first digitized into arrays of pixels, arranged in rows (horizontal line) and columns (vertical lines). As shown in figure 8,

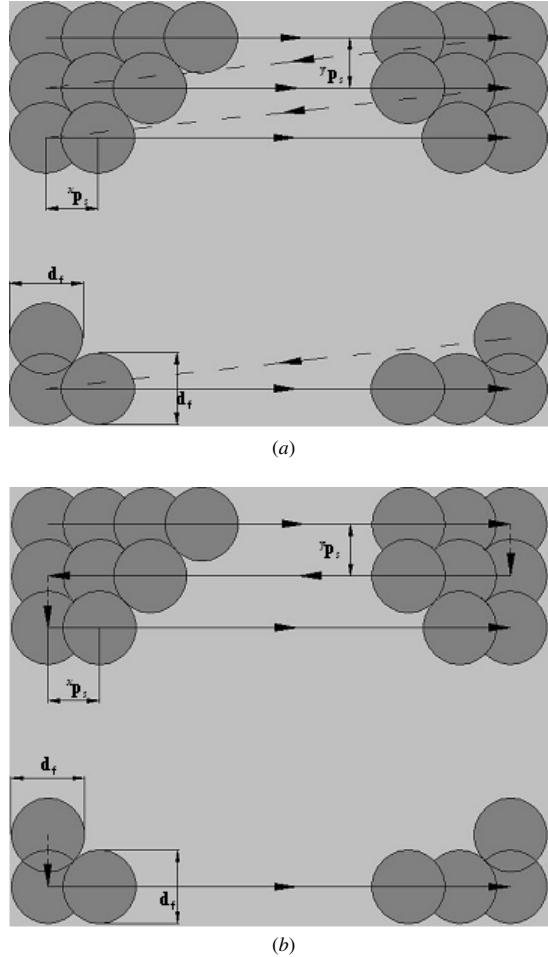


Figure 8. Scanning procedures with arrows indicating scanning direction: (a) raster scan; (b) serpentine scan.

two types of scanning procedure, raster and serpentine scans, are normally used to drive the FIB movement. They are performed in a sequential manner, one scan line after another. Figure 8(a) shows the raster scan while figure 8(b) illustrates the serpentine scan. In raster scanning, the scan moves in the same direction throughout the procedure. On the other hand, the serpentine scan direction is reversed after each scan or pass. In both figures, the solid line delineates the beam movement and milling can occur in any of the pixels scanned while the dotted line illustrates the path taken by the returning passes of the beam and no milling actions are taken in these segments. The arrows shown in the figure indicate the direction of scanning. Since the raster scan is the most commonly used scan procedure in computer graphics, each series of the horizontal pixels is also called a raster line or a scan line.

In very rare cases, some FIB machines used mainly for research have adopted a scheme called a vector scan to control the beam movement, in which the pattern is represented by a series of line segments. The coordinates of the beginning and ending pixels (or locations) of these line segments are stored in the computer memory and used through a digital-to-analog converter to drive the FIB. Because of its vast storage requirement in milling high-resolution microstructures, the vector scan is rarely used in commercial FIB machines. The vector scan is also known as a random scan in computer graphics.

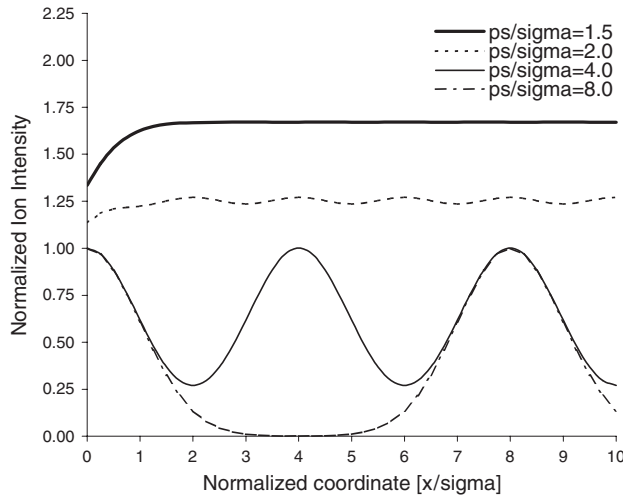


Figure 9. Overlap effect on ion flux distribution for Gaussian FIB milling.

In milling, both raster and serpentine scans are popular. For example, Yamaguchi *et al* (1985), Yamaguchi and Nishikawa (1995), Yongqi and Ngoi (2000) and Tseng *et al* (2002) adopted a raster scan in their research, while Ishitani *et al* (1991), Young *et al* (1993) and Steckl and Chyr (1999) used a serpentine scan to regulate the beam movement. No noticeable impacts on the resulting milled structures have been reported by just changing the scan from raster to serpentine or vice versa.

4.2. Uniform ion flux in scanning direction

To mill a smooth profile with a constant rate of material removal or milling rate, the ion intensity rate or ion flux with respect to the scanning direction has to be uniform or unwavering. To achieve this, the pixel spacing must be small enough to allow a proper overlap between adjacent pixels so that a smooth uniform profile can be milled. In addition, to mill a smooth surface between scan lines, the pixel spacing between adjacent scan lines must be also small enough to allow a proper overlap between adjacent lines. To simplify the presentation, obtaining a uniform ion intensity or ion flux with respect to the scanning direction is first discussed and then the conclusion is extended to include the uniformity between the scan lines.

The threshold value for the minimum amount of the beam overlap should be known first. The value can be determined as long as the intensity profile of the FIB can be mathematically defined. If the ion distribution of a FIB is approximated by a Gaussian distribution, as recommended by many investigators (Harriott 1990, Ben Assayag *et al* 1993, Edinger and Kraus 2000), the scanning ion flux becomes steady and unwavering when the normalized pixel spacing (p_s/σ) is smaller than 1.5, where σ is the standard deviation of the Gaussian distribution.

Figure 9 shows the normalized ion flux or intensity at different normalized pixel spacings (p_s/σ). The normalized Gaussian distribution is used to represent the FIB profile and the coordinate is normalized by the standard deviation, σ . As shown in figure 9, at $p_s/\sigma = 8$, the ion flux of milling resembles each individual Gaussian distribution and no

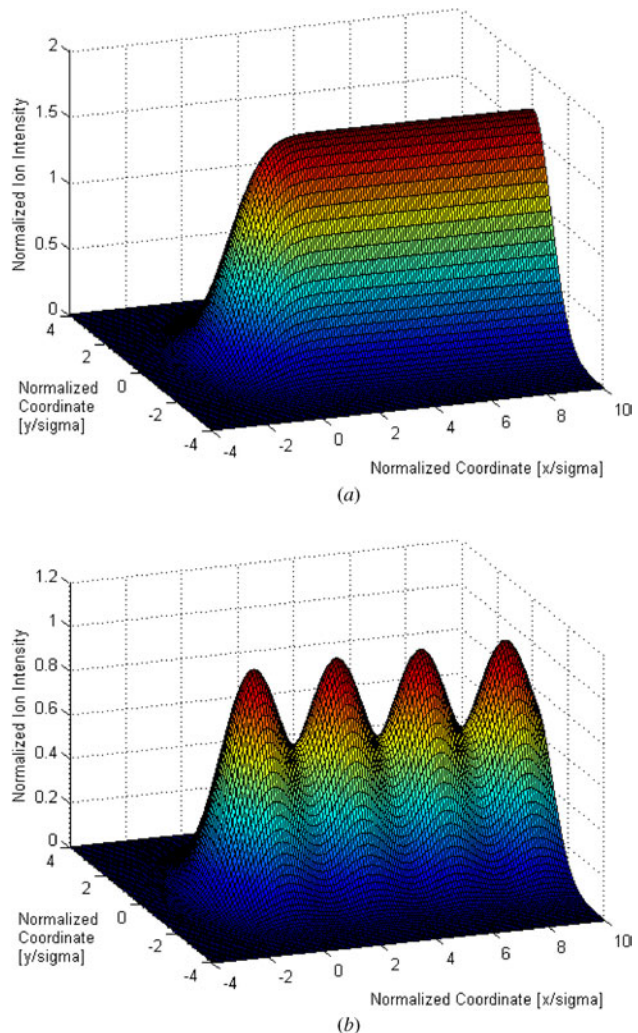


Figure 10. Normalized ion flux distribution along a scan line with normalized pixel spacing equal to (a) 1.5 and (b) 3.0.

(or immeasurable) overlap is observed, while a small portion of overlap is observed at the tail regions when p_s/σ reduces to 4. As p_s/σ decreases to 2, the fluctuation of the ion flux becomes less than 3% of its mean. Finally, the fluctuation disappears as p_s/σ reaches 1.5 and the normalized ion flux becomes stable and converges to a constant of 1.671, i.e. the fluctuation becomes immeasurable, less than 0.01%. For a Gaussian distribution beam, d_f is equal to 2.35σ (Weisstein 1999), the condition of $p_s/\sigma = 1.5$ is equivalent to $p_s/d_f = 0.637$. To clearly illustrate the ion flux distribution, the 3D profiles for p_s/σ equal to 1.5 and 3.0 are shown in figures 10(a) and (b), respectively. This clearly indicates that, in order to have a uniform scanning ion flux in channel milling, the normalized pixel spacing should be equal to or smaller than 1.5 (or $p_s/d_f = 0.637$).

4.3. Uniform ion flux along and across scanning lines

For the clarity of the presentation, the pixel spacings along and across the scanning lines are different and are denoted as ${}^x p_s$ and ${}^y p_s$, respectively. To consider only the across-line movement, the normalized pixel spacing (${}^x p_s/\sigma$) along

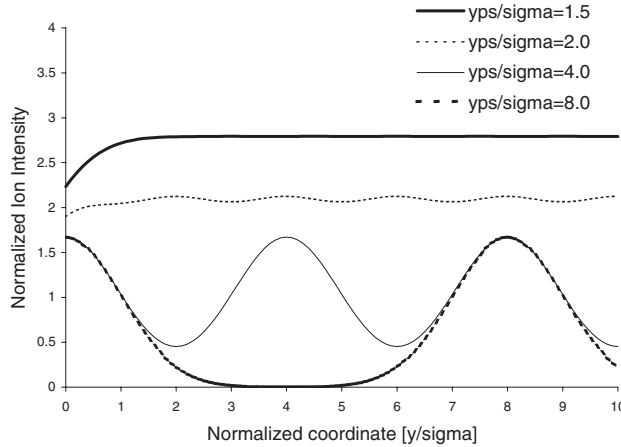


Figure 11. Normalized ion flux variation at several normalized $y p_s$, with normalized $x p_s = 1.5$.

the same scanning line should be assumed to be infinite and the corresponding normalized ion flux at different normalized across-line pixel spacings ($y p_s / \sigma$) should be similar to that shown in figure 9. If the across-line pixel spacing ($y p_s / \sigma$) is reduced to 1.5, the normalized ion flux at different ($y p_s / \sigma$) is shown in figure 11. As shown, the fluctuation decreases with decreasing ($y p_s / \sigma$) and the normalized ion flux becomes stable and converges to a constant of 2.792, as ($y p_s / \sigma$) reaches 1.5.

Again, the corresponding ion flux distribution can be clearly observed in 3D figures. The ion flux distributions shown in figures 12(a)–(c) are the conditions at ($y p_s / \sigma$) = 3.0 with ($y p_s / \sigma$) = 8, ($y p_s / \sigma$) = 1.5 with ($y p_s / \sigma$) = 8.0 and ($y p_s / \sigma$) = 1.5 with ($y p_s / \sigma$) = 1.5, respectively. The profile shown in figure 12(a) is similar to that of figure 10(b) and the only difference is the milling direction. As shown in figure 12(c), to have a uniform scanning ion flux in all of the areas considered, the normalized pixel spacings of both ($x p_s / \sigma$) and ($y p_s / \sigma$) should be equal to or smaller than 1.5 (or $x p_s / d_f = y p_s / d_f = 0.637$). Indeed, the uniformity condition of the ion intensity with respect to the scanning direction can be directly extended to satisfy the uniformity condition between the scan lines.

Also, as suggested by figure 12, a full drilling process for making an array of holes would require both the normalized pixel spacing to be larger than 8. As a result, the drilling process can be considered as a special case of channel milling. A brief mathematical derivation for the uniformity condition of the ion flux can be found in the appendix.

5. Microchannel milling using single pass

Microchannel structures have been fundamental building blocks for many microdevices, including micro heat pipes, sensors, optics and fluidic devices (Madou 1997, Tseng *et al* 2000). They are analogous to wires or thin-film electrical interconnects in conventional integrated circuits. Since the demand for smaller feature sizes of microdevices has increased, many studies on making nanoscale channels using FIB milling have been recently reported. For the sake of comparison, some of these nanochannel studies will also be

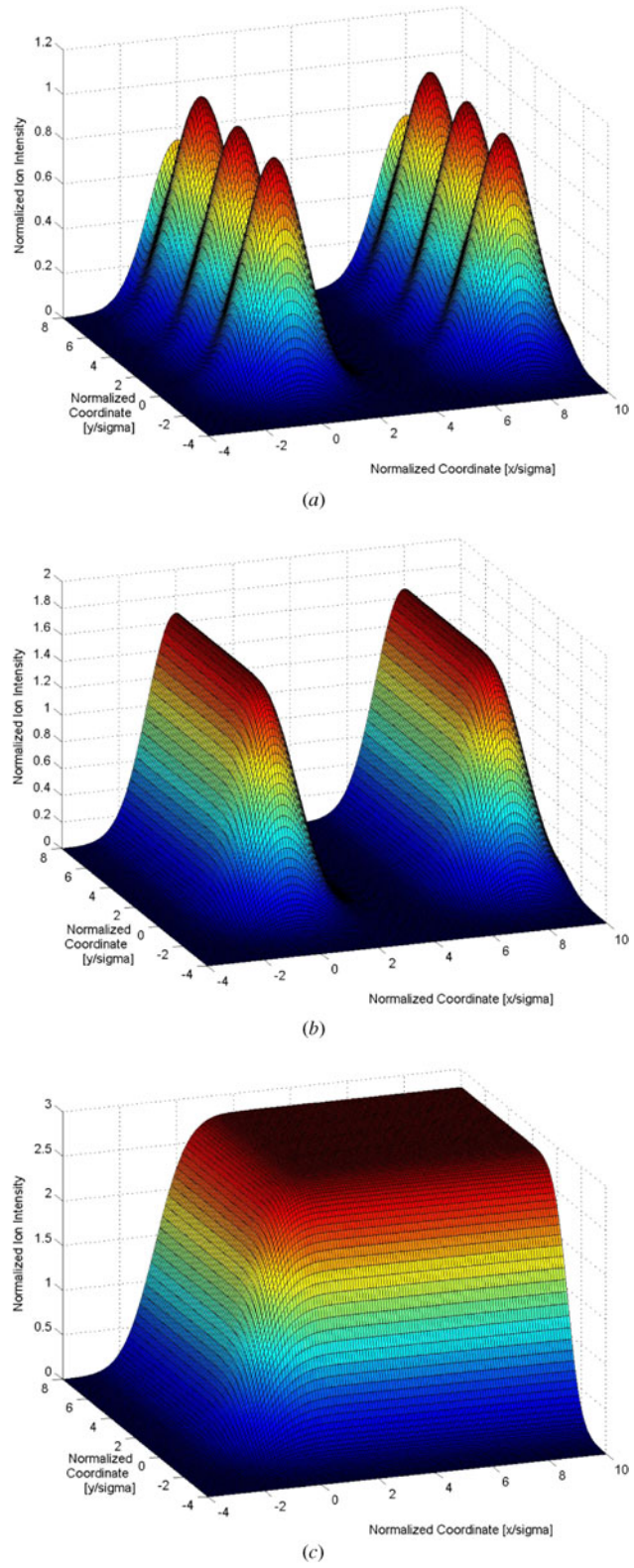


Figure 12. Normalized ion flux distribution in multiple scan-line milling: (a) normalized $y p_s = 3.0$ and normalized $x p_s = 8.0$; (b) normalized $y p_s = 1.5$ and normalized $x p_s = 8.0$; (c) normalized $y p_s = 1.5$ and normalized $x p_s = 1.5$.

discussed in this section. Typically, the beam current and diameter used for milling these nanochannels can be extremely

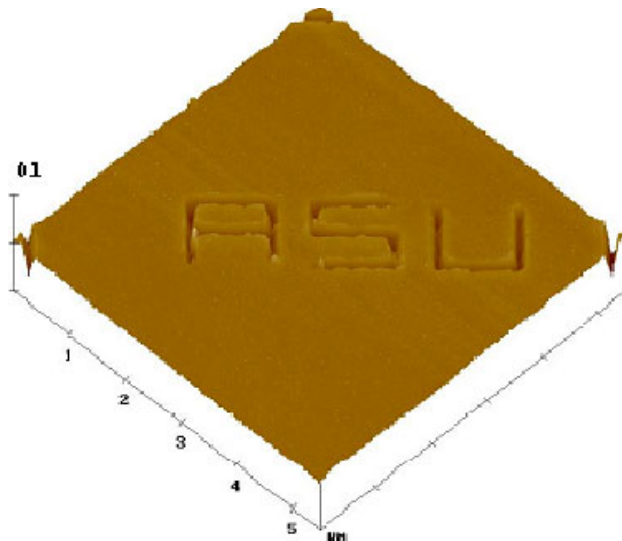


Figure 13. AFM image of ‘ASU’ pattern milled by 90 keV As^{2+} FIB with 5 ms dwell time.

small, of the order of 1 pA and 10 nm, respectively, with the dwell time of the order of 1 μs , a few orders of magnitude less than normally used for micromilling.

The FIB is an effective tool for prototyping microchannels. The sputtering yield cannot be directly used to determine the material removal rate in milling because of the problem of redeposition of sputtered materials (Fu *et al* 2000b, Lugstein *et al* 2003). To quantify the effect of redeposition, microchannels are frequently milled with a single pass and the profiles of the channels are measured to calculate the corresponding milling yield or rate.

5.1. V-shaped microchannel profiles

A set of submicrometer channels milled by a single pass has been studied by Tseng *et al* (2002). A 90 keV As^{2+} FIB with a beam current of 5 pA is used to mill a 125 nm thick gold film coated on a Si wafer. The pixel spacing (p_s) is set at 14.5 nm and the beam FWHM diameter (d_f) is set at 50 nm. Since the corresponding ratio of pixel spacing to beam diameter (p_s/d_f) is 0.29, which is smaller than the threshold value, 0.637, the scanning ion flux is steady and uniform. Using raster scanning, several different sizes of the abbreviation of Arizona State University: ‘ASU’ patterns are milled with the dwell time varying from 5 to 50 ms. A typical pattern milled with a 5 ms dwell time is shown in an atomic force microscopy (AFM) image depicted in figure 13.

The corresponding cross-sectional contour is shown in figure 14 indicating that the channels milled by a single pass possess a V-shaped profile with a maximum depth at the center and a maximum width at the mouth. Ridges are formed along the channel banks. The figure also shows that the four features are used to characterize the profile of the V-shaped channel: A is the ridge width, which is the distance between the ridge peaks; B is the mouth width, which is the channel width with respect to the original surface; C is the depth from the original surface; D is the ridge height. Tseng *et al* (2004) also found that, although all of the feature sizes increase with the dwell time varying from 5 to 50 ms, the increase rates of

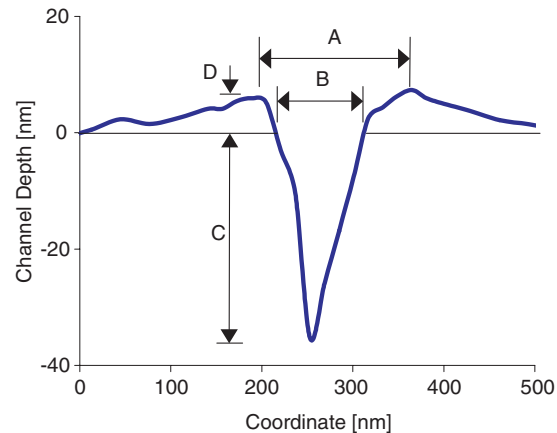


Figure 14. Feature definition and AFM measurement of channel profile milled with 5 ms dwell time.

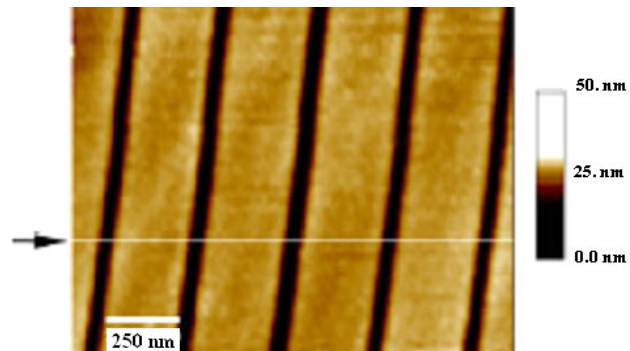


Figure 15. AFM image of channel pattern milled at 1 pA on Si substrate (after Li *et al* 2003).

the sizes are gradually reduced as the dwell time increases. This may indicate that a large amount of sputtered materials is redeposited into not only the ridge (outside the channel) but also inside the channel since the mouth width and the milling depth should increase proportionally with the dwell time without redeposition. Since only a single pass is used, the V-shaped channel is relatively shallow. The corresponding aspect ratio is of the order of 1/3 and is insensitive to the range of the dwell time considered.

Both Frey *et al* (2003) and Li *et al* (2003) have recently used a 30 keV Ga^+ FIB to mill nanoscale channels with a single pass on Si substrates. They used different beam diameters at different beam currents and learned that the channel profiles milled with a single pass are similar to that shown in figure 14, in a ‘V’ shape. One of the channel profiles milled at 1 pA with a beam diameter less than 10 nm reported by Li *et al* (2003) is shown in figure 15. It indicates that the V-shaped channel is approximately 10 nm deep and 65 nm wide. Their results further confirm that the V-shaped channel profile is the inherent shape obtained by single-pass FIB milling. Also, the measurements shown in figure 14 and reported by Li *et al* (2003) all reveal that the mouth width of the V-shaped channel can be much larger than the beam diameter (d_f) by almost one order of magnitude. This may suggest that, at longer dwell times, the ion intensity outside the core region of the FIB is sufficiently high to produce a sizable amount of sputtering.

5.2. Linearity of milling depth with ion dose

The nonlinear relationship between the milled channel depth and the dwell time (or ion dose) found by Tseng *et al* (2002) may not be consistent with the findings reported by Xiong *et al* (2001) and Li *et al* (2003). Xiong *et al* (2001) used a 30 keV Ga⁺ FIB in milling (Ni₈₀Fe₂₀) permalloy nanochannels and observed that the milling depth increases linearly with the dose density for depths less than 7 nm. On the other hand, Li *et al* (2003) studied the nanochannel profiles at several dwell times (0.1, 1, 10 and 100 μ s) and beam currents (1, 4, 11 and 70 pA) and found that the channel depth increases almost linearly with the ion dose but not with the dwell time for the beam currents considered. This is interesting because, if all other operating parameters are constant, the ion dose is proportional to the dwell time, i.e. the longer the dwell time, the higher the ion dose. In other words, the effects of the ion dose and the dwell time on the milling depth should be the same if single-pass milling is considered. Also, it may imply that the effect of redeposition may not be significant at low-energy milling so that the channel depth increases linearly with the ion dose or dwell time, since the ion energies employed by Xiong *et al* (2001) and Li *et al* (2003) are much smaller than those used by Tseng *et al* (2002). Consequently, these inconsistent observations make the effects of the dwell time or dose density on the milling depth a subject worthy of further study.

5.3. Milling yield

The nonlinear relationship between the milled channel depth and the dwell time does not mean that the cross-sectional area of milled channels increases nonlinearly with the dwell time. Tseng *et al* (2004) have used the channel dimension data shown in figure 14 to estimate the corresponding milling yield. They have found that the milling yield of using doubled charged As ions on an Au substrate is almost independent of the dwell time and is equal to about 22 atoms per ion, which is close to the value of the sputtering yield at the normal incidence predicted by TRIM. Since material removals are mainly dictated by both sputtering and redeposition in milling, it seems that, for the channel milling considered, the decrease in milling yields due to redeposition almost counterbalances the increase due to the incident angle. The milling yield is a measure of the material removal rate, which is proportional to the change of the cross-sectional area in single-pass uniform channel milling. It should be noted that, since the channels are milled by a single-pass procedure, the value of the ion dose can be easily estimated from equation (A3) reported in the appendix and the corresponding material removed during milling can be evaluated from the data similar to those shown in figure 14.

The fact that the milling yield is roughly equal to the normal incident sputtering yield has also been recently observed by other investigators. In single-pass channel milling, Lugstein *et al* (2003) used a 50 keV Ga FIB on a Si substrate and reported that the milling yield is 2.5 atoms per ion. It can also be found from figure 5 that the minimum sputtering yield at the normal incidence predicted by TRIM is also approximately 2.5 atoms per ion. Here the milling yield is defined as the number of the target atoms milled by one incident ion.

5.4. Swelling or amorphization

If the dose level of milling ions is not high enough, amorphization may occur in the bombarded area of a crystalline substrate and induce the substrate to swell. For a crystallized Si substrate bombarded by Ga ions, the dose level to cause amorphization is of the order of 10^{15} ions cm^{-2} , while the effective milling dose should be at least two orders of magnitude higher than the amorphization dose as indicated by Frey *et al* (2003) and Lugstein *et al* (2003). In amorphization, the incident ions in most cases are buried in the target material and may also displace the target atoms from their lattice sites so that the displaced atoms redeposit on the nearby surface. Since most of the FIB roughly resembles a Gaussian ion distribution, the intensity at the fringe (tail) of the beam is much smaller than that at the core (center region) and it is not strong enough to sputter materials but is sufficient to cause amorphization that induces substrate swelling. Normally, the intensity to cause swelling is two to three orders of magnitude lower than the optimized sputtering intensity and the swelling disappears if the intensity increases, as reported by Stanishevsky (1999), Frey *et al* (2003) and Lugstein *et al* (2003). During channel milling, the FIB always has a tail region that possesses the right dose to cause maximum swelling. The ridge height shown in figure 14 can be a result of both the redeposited materials and the swelling of the substrate. However, it is believed that the ridge consists mainly of redeposited materials, which increase in volume with increasing dwell times or ion doses.

6. Microchannel milling using repetitive passes

Three important features in microchannel structures are required for many applications: (a) flat channel bottom; (b) nearly vertical sidewalls; (c) high-aspect-ratio profile. As discussed in the preceding sections, V-shaped profiles are commonly milled by the single-pass procedure. This may imply that multiple repetitive passes are indispensable to mill channels with these three-feature requirements. The techniques related to multiple repetitive passes are reviewed in this section.

6.1. Single pass versus repetitive pass

In FIB milling, the initial sputtered channel profile reflects the current density distribution of the beam if the beam impinges on the target normally. For the consequent beam impingements, because of the effects of redeposition of the sputtered materials, the channel grows deeper but also narrower. Since the sidewalls are slanted, the effects of the angular dependence of the sputtering yield also come into play. A flat bottom, which is important for engineering applications, can be achieved by repetitive-pass milling on the target area in order to remove the redeposited materials. In control of the first beam pass, either a raster or serpentine scan is used to trace all the regions to be milled. Then, a repetitive pass is applied following the pass milled previously.

Yamaguchi *et al* (1985) studied the effects of using single and repetitive passes on milling a Si substrate, as shown in figure 16. A $10 \times 10 \mu\text{m}^2$ cavity was milled using a raster scan with 300 parallel scanning lines. A Ga⁺ FIB with an

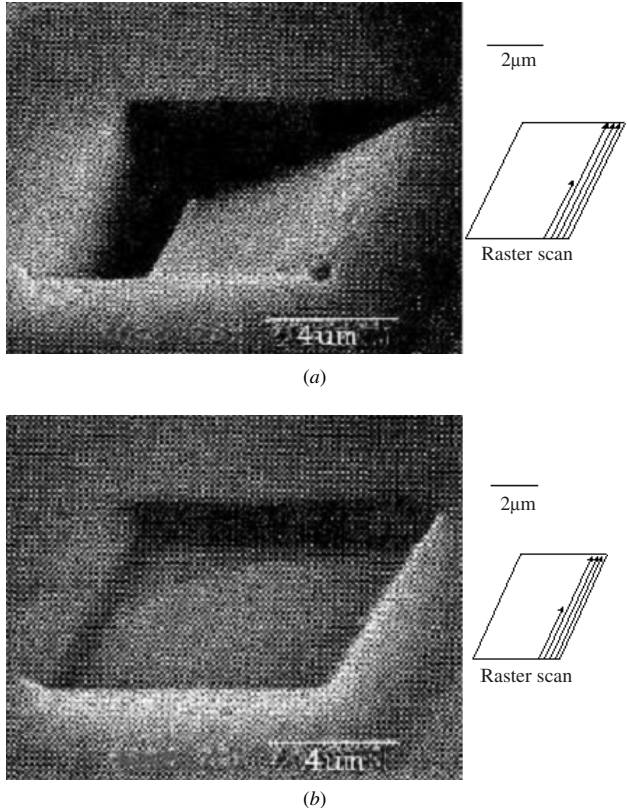


Figure 16. SEM photographs of Si pattern milled by 30 keV Ga^+ FIB at a total dose of 1.9×10^{18} ions cm^{-2} : (a) slow single pass at 2 s per line with 300 scan lines; (b) fast (200) repetitive passes at 10 ms per line with 300 scan lines (after Yamaguchi *et al* 1985).

accelerating voltage of 30 keV and 0.5 nA beam current was used. In the first case as shown in figure 16(a), the scanning speed is slow at one half line per second (or $5 \mu\text{m s}^{-1}$) and a single-pass milling scheme was utilized, while in the second case as shown in figure 16(b), the scanning speed is 200 times faster (1 mm s^{-1}), so that the cavity was milled by 200 repetitive passes. Since the total dwell times are the same, the total doses are the same for both cases at 1.9×10^{18} ions cm^{-2} . In the first case, a cavity with an inclined bottom was observed and the depth of the cavity at the end of the milling is far deeper than the depth where the milling is started. It is believed that the inclined bottom is caused by redeposition. Because the sputtered materials are continuously redeposited into the region milled earlier, the redeposited materials accumulate more on the regions milled earlier in the pass. In the second case, the bottom of the milled cavity is nearly flat and the sidewalls are almost vertical. In this repetitive-pass scheme, the amount of sputtered materials in each pass is small and the redeposition to other regions is not only proportionally smaller but also is removed equally in the subsequent pass. This is the main reason that a repetitive-pass scheme can lead to more uniform milling. This study has also shown that two milling strategies using identical ion beams with identical total dose and pixel spacing can result in significantly different channel profiles.

It is noted that milling an inclined surface due to redeposition is not always undesirable. Ishitani *et al* (1991) demonstrated that the redeposited materials can be used to

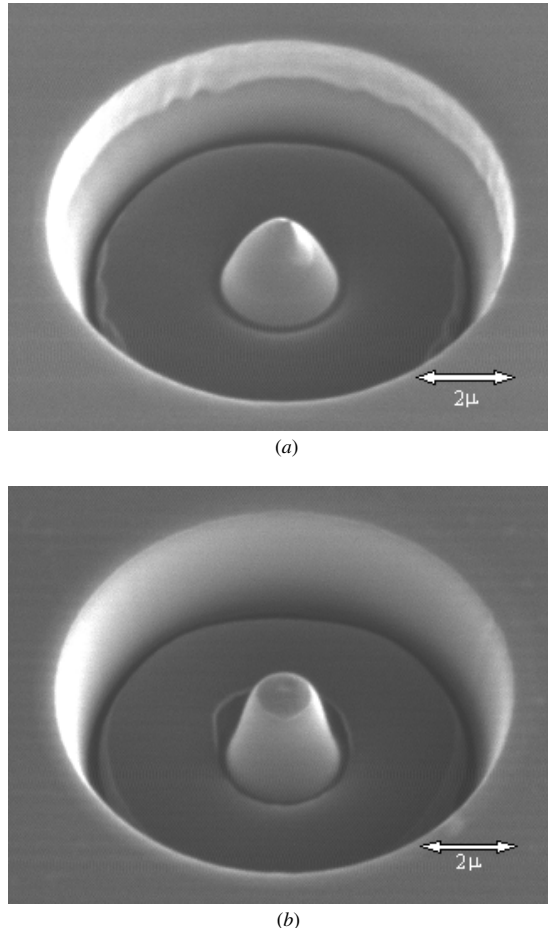


Figure 17. Tip structures milled by Ga^+ FIB with a total dose of 15 nC cm^{-2} : (a) using a single pass; (b) using four repetitive passes (courtesy of Yongqi and Bryan 2000).

adhere a chip with dimensions of $2 \times 5 \times 6 \mu\text{m}^3$ to the milled Si substrate with potential applications for wafer-level-scale integration or packaging. Using a slow single-pass milling, two wedges or slant surfaces toward each edge of the chip can be formed by the redeposited materials. It has been shown that the wedges provide a good mechanical connection between the chip and Si substrate.

Both single-pass and repetitive-pass schemes have been used by Yongqi and Bryan (2000) to study the effect of the number of the pass on the slope of the structure milled. A 20 keV Ga^+ FIB with an aperture diameter of $250 \mu\text{m}$ was used to mill two tip structures in a cavity with the same total dose of 15 nC cm^{-2} . The annular cavity shown in figure 17(a) is milled by a single pass and has an outer diameter of 6.2 nm and a depth of 4.9 nm, while the structure shown in figure 17(b) is achieved by four repetitive passes with an outer diameter of 6.1 nm and a depth of 4.7 nm. As shown in the figure, changing from a single-pass scheme to a repetitive approach enlarges the diameter of the tip or increases the slope of the cone. The main reason is that if the beam size and total ion dose are kept the same, increasing the number of passes can decrease the effects of redeposition as discussed earlier. Using repetitive passes, the redeposition will be proportionally reduced in each pass and a portion of the redeposition from the earlier passes can be removed by the subsequent milling. Consequently, in milling

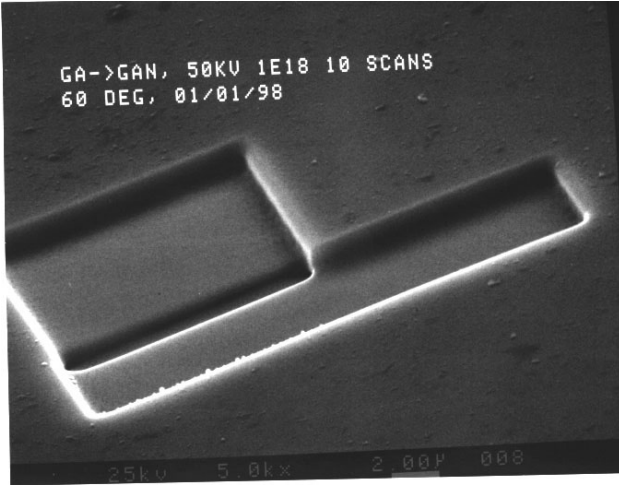


Figure 18. SEM photograph of GaN pattern milled by 90 keV Ga⁺ FIB at normal incidence and ten repetitive passes (courtesy of Steckl and Chyr 1999).

a tip component, the number of passes can be used to adjust the profile of the tip or the slope of the sidewalls.

6.2. Flat and vertical channels

As shown in the scanning electron microscopy (SEM) photograph in figure 18, Steckl and Chyr (1999) used a serpentine scan to mill an L-shaped pattern in which the deeper channel is obtained by the overlap of the two rectangular patterns. The total area of the pattern is about 200 μm² on a 20 μm thick GaN film, which is grown by hydride vapor phase epitaxy on a sapphire substrate. The non-overlap region is about 2 μm deep so that the GaN film should be thick enough to ignore any possible substrate effects. The pattern is milled with ten repetitive passes using a 90 keV Ga⁺ FIB with a dose of 10¹⁸ ions cm⁻². The beam scans at normal incidence with a speed of 42 μm s⁻¹. In a serpentine scan, the scan direction is reversed after each pass to minimize redeposition effects, and thus sharply defined regions with a uniform depth and smooth surface can be milled.

6.3. Microchannels with high aspect ratio

The ability to make high-aspect-ratio microstructures is becoming increasingly essential and a leading factor in the success of manufacturing microdevices or systems (Tseng *et al* 2000). Recently, Lugstein *et al* (2003) have used a 50 keV Ga⁺ FIB to mill nanochannels of various aspect ratios to investigate the impact of shrinking feature size on milling efficiency. At relatively low dose intensities ranging from 10¹³ to 6 × 10¹⁵ ions cm⁻², swelling in the Si substrates was observed because of amorphization. The maximum swelling size of 3 nm was found in the neighborhood of 10¹⁵ ions cm⁻². Higher dose intensity leads to material removal with a yield of 2.5 Si atoms per Ga ion. They found that shrinking critical dimensions led to higher sputtering yield, which is attributable to the self-focusing effects of incident ions becoming dominant at aspect ratios of the order of 1. At higher aspect ratios, redeposition is again the dominant effect.

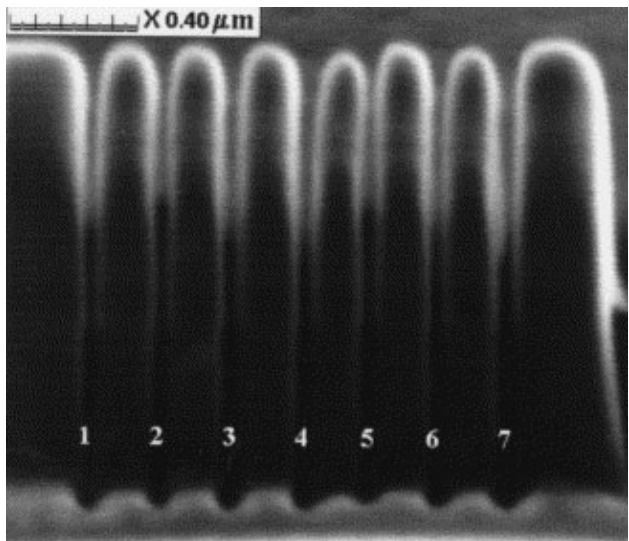


Figure 19. FIB milled channels with the widths of 30–40 nm and depths of 540–870 nm (after Stanishevsky 1999).

Stanishevsky (1999) has also used a FIB of 50 keV Ga⁺ ions to mill various patterns on tetrahedral amorphous carbon (ta-C) films for optical and microelectronic applications. He found that the slope of the sidewalls of milled channels is affected by the beam current and it changes from 70° to 88° as the beam current drops from 700 to 3 pA. It is believed that the beam tail rounds the edges of the milled structures and limits the resolution of the channels. With higher slopes of the sidewall, the channels with higher aspect ratios can be milled. A lower beam current can also produce channels with a finer quality, but the number of repetitive passes required to mill the channels is much higher, which can significantly reduce the productivity.

One of the patterns produced by Stanishevsky (1999) consisting of seven channels is shown in figure 19. The beam currents used in milling these seven channels are very small, varying from 1.8 to 3 pA, with a pixel spacing (p_s) of 10 nm and a beam diameter (d_f) equal to or less than 12 nm. With reciprocal repetitive passes, the total dose varies from 20 to 50 nC μm⁻², while the dwell time for each pass changes from 1 to 50 μs. The higher the dose, the deeper the channel can be milled. As shown, the channel widths marked 1, 2, 5 and 6 in figure 19 can be as small as 30 nm and the respective depths are 660, 540, 570 and 800 nm. The corresponding aspect (depth-to-width) ratios for the deepest channel can be higher than 25. The milling rate is lower when channels become deeper. Some rounding of the edges and slightly sloped sidewalls in the seven channels milled are observed even at such low beam currents. It should be noted that the typical aspect ratio made from a standard semiconductor wet etching process is of the order of 1. It should be noted that, in the present milling operation, the possible ratio of the pixel spacing to the beam diameter (p_s/d_f) can be as high as 0.83, which is larger than the threshold value of 0.637 and is not small enough to provide enough beam overlap for smooth ion flux, as illustrated in figure 9. This may be the main reason that the sidewalls shown in figure 19 are not straight or smooth.

Chyr *et al* (1999) have used a 70 keV Ga⁺ ion FIB to mill a GaN Bragg grating mirror as shown in the SEM

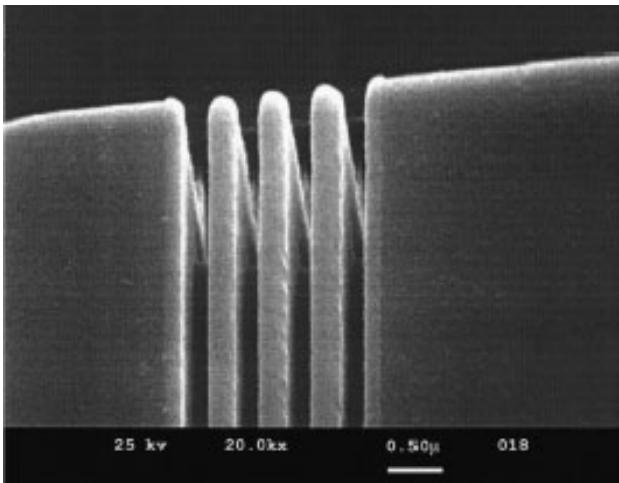
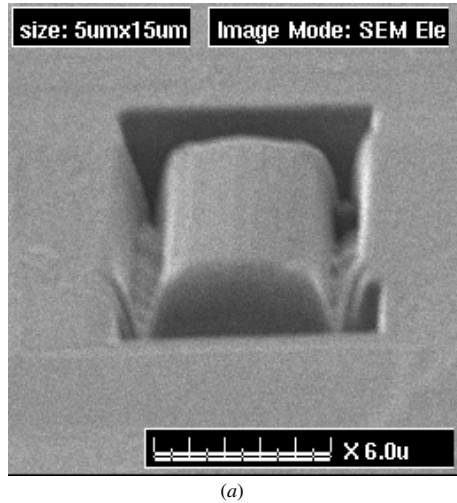


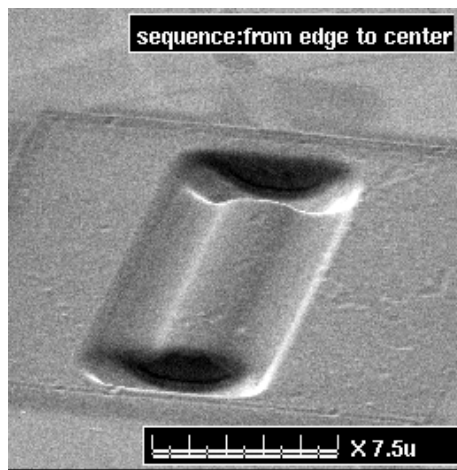
Figure 20. SEM photograph of GaN DBR grating with a period of 500 nm and spacing of 150 nm (courtesy of Chyr *et al* 1999).

photograph in figure 20. The FIB current is ~ 22 pA with many dozens of repetitive passes to achieve a constant dose of 3×10^{18} ions cm^{-2} . The grating mirror shown in the SEM photograph is designed for a lasing wavelength of 370 nm with a grating period of 500 nm and a spacing of 150 nm. This type of mirror, also known as the distributed Bragg reflection (DBR) grating mirror, can offer better reflectivity than the conventional cleaved mirrors needed for short cavity lasers. The depth of the DBR grating is close to 2 μm , which makes the aspect ratio (the ratio of the depth to spacing) higher than 10. Figure 20 further indicates that the FIB can fabricate a very high-aspect-ratio grating structure with the required surface and dimension qualities for the laser device.

In high-aspect-ratio milling, the channel depth is frequently required to be controlled within the prescribed dimensions and tolerances. Consequently, the ability to detect the endpoint or channel size during processing within the required accuracy becomes critical (Harriott and Vasile 1989, Latif *et al* 2000). Since the milling rate for each pass is minute and fluctuant, and the repetitive passes are necessary for high-aspect-ratio structures, the ordinary way to use time duration or pass number to predict the depth of cut becomes impractical and inaccurate. Various techniques, including the use of absorbed sample current, photons (Yamaguchi *et al* 1998), secondary electrons (Davies and Khamsehpour 1996), secondary ions (Nojima *et al* 2002) and electric resistance of milled track (Latif *et al* 2000), have been developed for on-line depth detection with nanometer scale precision (Bischoff *et al* 2001). Davies and Khamsehpour (1996) studied the correlation between the absorbed current and the secondary electron as a function of the FIB dwell time and found that the detection accuracy can be significantly improved by reducing the dwell time. However, each technique can have advantages for a specific application but disadvantages for other applications. In general, the milling characteristics, including the aspect ratios of milled geometry, the redeposition and the beam properties as well as the milled surface features, including texture, flatness and finish, can all affect the signal detectability. A combination of these techniques may be necessary to obtain a more reliable measurement.



(a)



(b)

Figure 21. Comparison of two different scan sequences: (a) sequence from center to edge; (b) sequence from edge to center (courtesy of Fu and Bryan 2001).

7. Microstructures with controlled profiles

Many FIB techniques have been developed to mill more complicated 3D microstructures than those microchannels presented in the previous sections. In general, it is still a great challenge to mill high-precision 3D structures with arbitrarily predefined cross-sectional profiles. This can only be accomplished by precisely controlling the material removal rate at each pixel and by developing a strategy in each pass to alleviate or compensate for the effects of redeposition. In this section, the effects of altering the scanning sequence on redeposition in milling curved structures will be examined first. The processes used to mill different 3D microstructures with controlled profiles will then be presented.

7.1. Scanning sequence

Fu and Bryan (2001) recently studied the redeposition effects of milling BK7 glass curved substrates by considering two different scanning sequences. As shown in figure 21(a), the glass structure is milled with the sequence initiated at the center and ended at the edge, while the microstructure in

figure 21(b) is obtained by a sequence from the edge to the center. By comparing these two structures, it is observed that two different structures can be produced by just reversing the scanning sequence, which can result in different redeposition patterns. Roughly speaking, the earlier the region is milled, the more the redeposited material is accumulated in that same region. As a rule of thumb, the region where a greater milling depth or more material removal is desired should be milled last in the scanning sequence. If a curved structure similar to that shown in figure 21(a) is desired, more materials have to be removed at the edge and thus the edge region has to be milled last while the center region should be milled first. The sputtered materials are then redeposited into the center when the edge region is milled, thus resulting in a structure with redeposited material piling at the center and a deep trench at the edge. The open space left in earlier milling in the center should be designed for compensating the redeposited materials milled later. Since milling a shallow region takes less effort than milling a deep region, milling a shallow cavity at the center for compensating the redeposited materials is much more effective than milling a deeper trench in the edge when the center region is milled last in the sequence. Both structures shown in figure 21 were milled on an area of $7.5 \times 10 \mu\text{m}^2$ with a raster scan procedure. A 50 keV Ga⁺ FIB with a beam current of 8.66 nA was used.

7.2. Annular patterns

Vasile *et al* (1999) developed a technique to control the dwell time at each pixel for milling microchannels with curved profiles. They reported a SEM image of a channel with hemispherical cross-sections on a silicon (100) substrate, as shown in figure 22. The channel is milled by a Ga⁺ FIB operated at 20 keV with a FWHM beam diameter of 619 nm and a beam current of 2.15 nA. As shown in figure 22(b), there is about 15% maximum deviation between the requested (designed) and the resulting milled profiles. The authors reported that the main reasons for this difference are due to the redeposition and the instability or drift of the beam current. However, no quantitative measurement of redeposition rate or beam current instability is given. Using the basic geometry shown in figure 22, axisymmetric sinusoidal wave channels can be fabricated in a Si substrate, as depicted in figure 23. The channel pattern starts by outlining an annular pattern having a 15 μm outer diameter with four periods of oscillation (Vasile *et al* 1999).

A similar annular pattern with continuous relief was also made by Yongqi and Nogoi (2000), who used a 50 keV Ga⁺ FIB to mill a 3×3 diffractive optical element (DOE) array in a Schott BK7 glass substrate, as shown in figure 24. Each element or lens has an outermost diameter of 8 μm and a singlet DOE of 500 nm with a focal length of 4.8 μm and a designed wavelength of 635 nm. Following a raster scan procedure, the milling is performed using a pixel spacing (p_s) of 13.7 nm with a beam diameter of 215 nm and a current of 8.66 nA. The corresponding normalized pixel spacing (p_s/σ) is 0.15, which is much less than 1 and should yield a very smooth ion flux, as discussed earlier. Yongqi and Nogoi (2000) also reported that the surface and dimensional quality of the optical elements is dependent on the beam size; the smaller

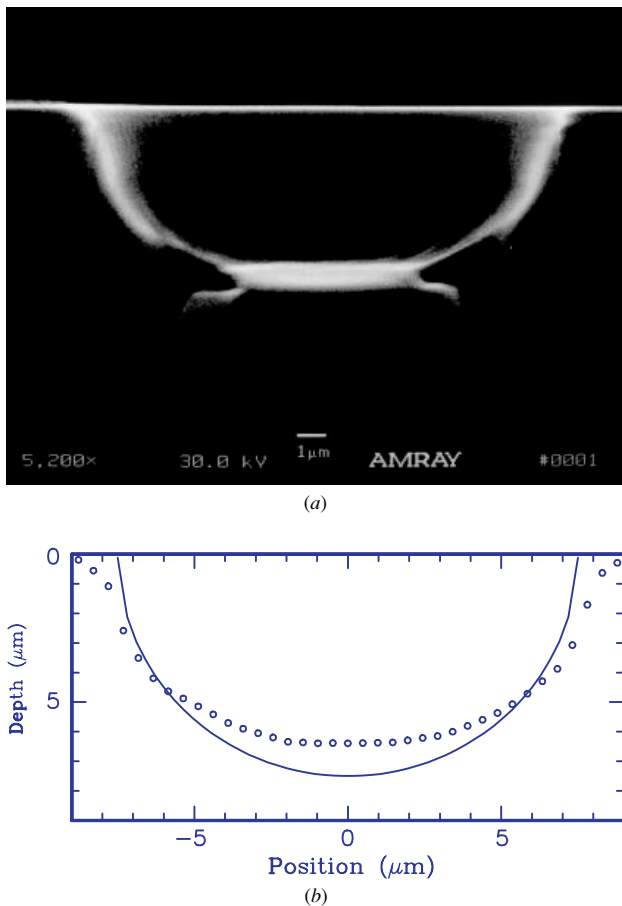


Figure 22. Cross-section profiles of a hemisphere microchannel: (a) SEM image of milled hemispheric microchannel; (b) comparison between specified (solid line) and milled (circles) profiles (courtesy of Vasile *et al* 1999).

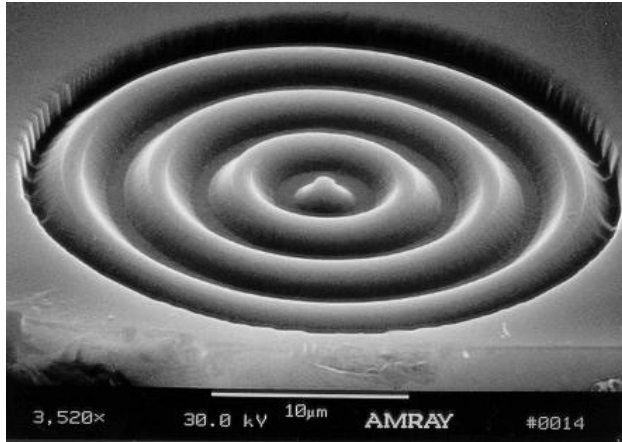


Figure 23. SEM image of sinusoidal annulus microchannels viewed at 60° (courtesy of Vasile *et al* 1999).

the beam size, the better the quality. Microlens arrays have applications in optical interconnects, multiple spot scanning microscopy, laser-to-fiber coupling, and numerous other areas in which geometrically precise arrays are required. Compared with the reflow of a photoresist island and laser writing, FIB technology has the advantages of higher resolution and more accurate relief control.

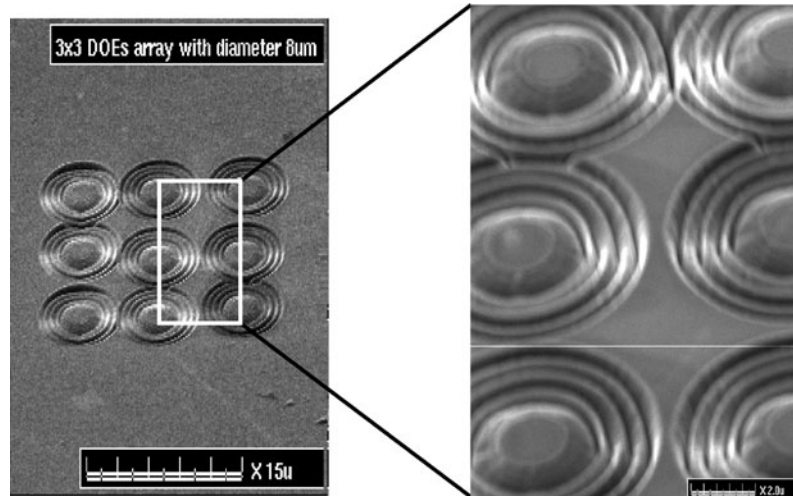


Figure 24. SEM micrograph of a 3×3 microlens array with focal length of $4.8 \mu\text{m}$ and designed wavelength of 635 nm (courtesy of Yongqi and Ngai 2000).

7.3. Tip structures

In addition to the microtip structure milled by Yongqi and Bryan (2000) shown in figure 17, Hopkins *et al* (1995) used a Ga^+ FIB to mill a sharp scanning probe microscope tip, as shown in figure 25. A 20 keV Ga^+ ion beam with a diameter of roughly 200 nm was used in the vector scanning of an annular pattern across the apex of an electrochemically etched wire. As shown, this method can produce an exceptionally sharp conical tip having a radius of curvature of 5–10 nm and widening to a diameter of 300 nm at a distance of $1 \mu\text{m}$ from the apex. Note that the removal of material during milling is not completely uniform. It has been found that the rim surrounding the central spikes is jagged and the central spikes themselves terminate in unusually sharp protrusions or microtips. In this case, it is believed that if a smaller beam with a lower current is used, the uniformity of material removal during milling can be improved.

In a separate work, Ishitani *et al* (1991) used a FIB to mill a microscale copper needle with two square pillar-like areas not far from the tip. They also used a FIB to trim a V-shaped cantilever tip for AFM. Ganpule *et al* (1999) have adopted the FIB to fabricate a ‘tip’-shaped ferroelectric capacitor structure with a size down to 100 nm. This ferroelectric capacitor is fabricated for testing the size effects on the ferroelectric properties.

7.4. Mechanical components

Fu *et al* (2000a) have developed a computer-aided system for their Micrion 9500EX FIB machine for direct milling of 3D microstructures. In this system, the popular AutoCAD file format can be used after data conversion. The Micrion machine uses Ga^+ ions with an energy of 5–50 keV and a probe current of 4 pA–19.7 nA. For the smallest beam currents, the beam can be focused down to 7 nm in diameter. By providing the relationship of the milling depth as a function of the major operating parameters, including the dwell time, the ion dose and the beam size, the computer-aided FIB system can precisely remove materials on a submicrometer scale at



Figure 25. SEM image of FIB-milled Ir probe showing a sharp spike at the apex (after Hopkins *et al* 1995).

each pixel, as reported earlier by Fu *et al* (2000c). Following a raster repetitive scan procedure, the computer-aided control system using the digitized CAD input file can mill various 3D structures. Fu *et al* (2000a) reported a gear structure milled with an ion dose of $5 \text{ nC } \mu\text{m}^{-2}$ and a beam aperture size of $150 \mu\text{m}$. As shown in figure 26, the gear has a root diameter of $11.3 \mu\text{m}$ and the geometry is originally designed in AutoCAD and is converted to the standard FIB XBM format. Although the shapes are complicated and a large ion beam aperture size is used, the manufactured structure still has a smooth peripheral edge. Such structures are very difficult to create directly by the standard XBM editor used by a typical Micrion machine.

In a similar attempt, Ishitani *et al* (1991) used a beam current of 10 nA and a beam diameter of 500 nm to mill

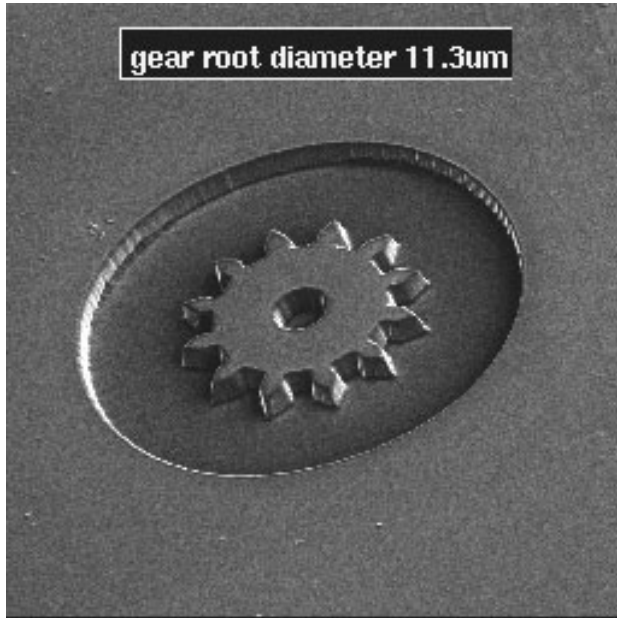


Figure 26. SEM image of gear structure milled with an ion dose of $5 \text{ nC } \mu\text{m}^{-2}$ (courtesy of Fu *et al* 2000a).

a stainless-steel microgear with a diameter of $45 \mu\text{m}$ and a thickness of $2 \mu\text{m}$. Compared with the conventional semiconductor, the authors claimed that FIB milling is much simpler.

For ultra-precision turning applications, Picard *et al* (2003) have used FIB milling to shape a micro lathe tool from a diamond tool blank, as shown in figure 27. The diamond is first brazed into a tapered tungsten carbide mandrel, and then ground to a tip having an approximate $40 \times 40 \mu\text{m}^2$ cross-section as shown in figure 27(a). The tool cutting edges are fabricated on the last $\sim 30 \mu\text{m}$ near the tip. As shown in figure 27(b), the width of the tool after milling is $23 \mu\text{m}$ and the single cutting edge is formed by the intersection of two ion-milled facets with a curvature of 40 nm approximately. This tool is made to have a small side rake angle (2°) and relief behind all cutting edges. As shown in figure 27(c), a double-tip microtool can also be shaped from a similar blank, having two rectangular tip surfaces $12 \mu\text{m}$ long and $10 \mu\text{m}$ wide separated by $7.7 \mu\text{m}$. While the right tip in figure 27(c) is $29 \mu\text{m}$ thick, the left tip is $26.5 \mu\text{m}$ thick. The variation in thickness is a result of the original cross-section of the tool blank and its orientation to the ion beam. Nevertheless, relief is established behind all cutting edges on this two-tip tool. It is expected that shaping of similar two-tip diamond tools on this scale would be virtually impossible by conventional methods such as grinding. A 20 keV Ga^+ ion beam with a beam size of 500 nm and 2 nA current is used in the milling operation.

During milling, the tool blank shown in figure 27(a) is mounted on an x - y stage which has a submicrometer motion resolution and can rotate 360° with 0.37° increments. Equipped with a computer-numerical control (CNC) system, which is similar to those used in a regular CNC turning center, the FIB system developed can mill very complex face geometries for making different types of microtools, as reported by Adams *et al* (2000). Picard *et al* (2003) also

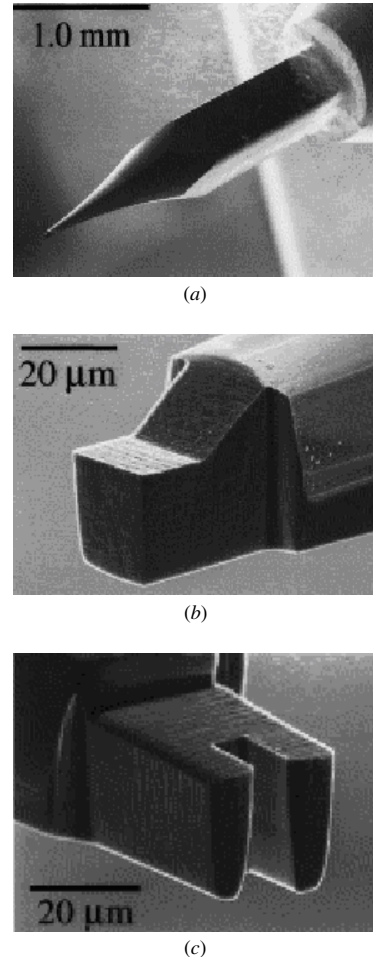


Figure 27. FIB milled micro diamond tool: (a) initial diamond tool blank in which the tool cutting edge is near the tip; (b) SEM image of FIB-shaped facets of a single-tip tool; (c) SEM image of FIB-shaped facets of a double-tip tool (after Picard *et al* 2003).

found that the quality of the present diamond tool geometry, including the roughness and tolerance, is similar to that of the steel and tungsten carbide tools made earlier, although the milling rate presently used is much lower than that used earlier.

Milling can also serve as a post-fabrication tool in studying the effects of the geometry variation on the mechanical properties. Fabian *et al* (2000) used FIB milling to modify the geometry of a microcantilever array to study the effect of the geometry change on the essential mechanical properties, including resonance frequency and temperature distribution. As shown in figure 28, the Si array consists of five $464 \mu\text{m}$ long cantilevers with a rectangular cross-section of $74 \times 5 \mu\text{m}^2$. The microcantilever array is originally fabricated by the standard semiconductor lithographic processes. Four of the five cantilevers are modified by locally milling using a 30 keV Ga^+ FIB with a beam diameter of 100 nm at 1 nA current. At such conditions, the typical material removal rate is $12 \mu\text{m}^3 \text{ min}^{-1}$. The enlarged view in figure 28 shows that a U-shaped notch with a depth of $4 \mu\text{m}$ and a width of $15 \mu\text{m}$ at the mouth is milled to lower its resonance frequency by 42%.

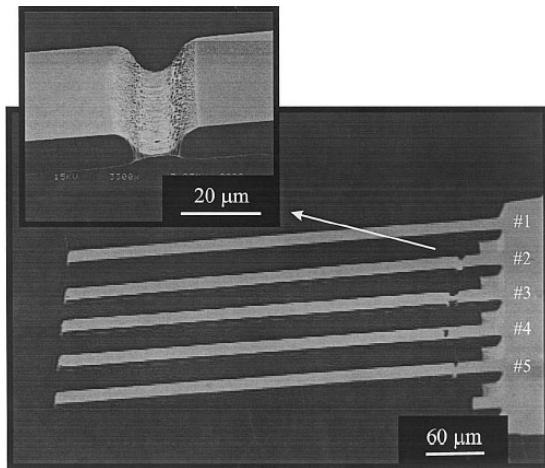


Figure 28. SEM image of modified cantilever array (after Fabian *et al* 2000).

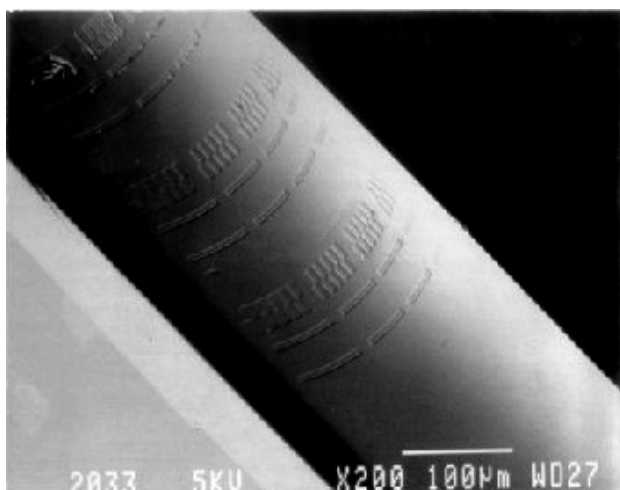


Figure 29. Flexible cylindrical fiber-based neural recording and stimulating electrode implants (courtesy of M Mitan *et al*, <http://www.eas.asu.edu/~fib/projects.htm>).

7.5. Curved substrates

At Arizona State University, work is currently underway to utilize an As⁺⁺ FIB to mill patterns on non-planar surfaces. The depth of focus of current optical steppers is a fraction of the resolution, making it practically impossible to pattern fine features on non-planar surfaces. The FIB is capable of a depth of focus an order of magnitude higher with a 50 nm resolution. Therefore, under proper working conditions, the FIB can offer the same, or better, patterning resolution over practically 180° of a cylinder several hundred of micrometers in diameter without the need for ‘rotation’. An example of some preliminary resist exposures across the circumference of a 250 μm quartz fiber coated with 10 μm of polyimide is shown in figure 29 (Mitan *et al* 2003). The goal of this effort is to fabricate an implant structure that is rigid enough to be inserted at any depth in the brain, yet flexible enough to conform to the brain tissue environment and remain stable in this position for chronic recording. The use of cylindrically symmetric fibers for this purpose also

allows the electrodes to have symmetrical monitoring access for 360°.

As discussed earlier, Adams *et al* (2000) and Picard *et al* (2003) have developed a computer-controlled stage for targets to not only move in the *x*- and *y*-direction but also rotate in the θ direction. They have demonstrated that, with this stage, a variety of microtools can be FIB milled from cylindrical substrates or objects. Two of these microtools are shown in figure 27. Ruchhoeft *et al* (1999) also developed stages with rotating or tilting abilities for lithographing microstructures in curved substrates and microstructures with curved surfaces.

8. Conclusions

The direct write FIB technology has several advantages over contemporary micromachining techniques, including better feature resolution with low lateral scattering and capability of maskless fabrication. An overview has been presented of the applications of the FIB technology in microfabrication using the direct milling technique. A variety of recent developments in FIB milling technology as well as emerging applications for optics, magnetics and electronics fields have been presented to illustrate its versatility and potential.

After presenting the recent development of FIB systems used for milling, the two governing phenomena of milling, sputtering and redeposition are specifically examined with the intent to provide guidelines for selecting operating parameters, including ion species, incidence angle and ion energy, for milling a specific substrate material. The effects of scanning strategy or sequence on the final milling shapes are assessed. The successful millings of a wide spectrum of high precision microstructures reviewed have demonstrated that the FIB milling is a vital alternative to other microfabrication processes.

Several general findings can be summarized here. Uniform input of ion intensity is the first step to mill a uniform profile and, to achieve this, the specific operation condition of the normalized pixel spacing has to be smaller than 1.5. The present review has also indicated that if throughput is not the issue, an ultra small amount of materials can be removed from the substrate using extremely small beam diameters (of the order of 10 nm) and currents (of the order of 1 pA) and high-precision devices or structure with resolutions of the order of 1 nm can be milled. Although milling is governed by both sputtering and redeposition, many studies have shown that the effect of redeposition often counterbalances the increase in milling yield due to the incident angle. As a result, the milling yield is close to the value of the normal incident sputtering yield. The single-scan (or pass) milling is an effective process to fabricate V-shaped channels or cavities with inclined bottom surfaces, while the repetitive-scan procedure is indispensable for making cavities with vertical sidewalls and flat channel bottom or making any high-aspect-ratio or curved structures. Last but not least, when milling a curved structure, a repetitive scan with a good strategy in selecting the scanning sequence is necessary. The scanning sequence should initiate at regions where the least amount of material or the smallest milling depth is desired and terminate at regions where the most amount of material or the largest milling depth is desired. This is mainly

due to the fact that the region milled earlier in the sequence accumulates sputtered materials from the region milled later.

While the progress in FIB equipment and process continues, the ability to control the depth of cut (milling) to the tolerances of the order of nanometers is still the most critical factor in milling high-precision components. Consequently, it is inevitable to have a feedback system to control the milling rate. A feedback signal that detects or monitors the milled shape in nanoscale accuracy during operation becomes a necessity. A reliable FIB system with the capability for endpoint detection or *in situ* monitoring should be developed further. The monitoring system in the current commercially available FIB system is still in its infant stage, as concluded in this review. Other product qualities, such as flatness, texture and surface finish, can also be important in many applications and the *in situ* detection systems may also be worth investigation.

Finally, FIB technology is still relatively young compared with other semiconductor fabrication processes. One of the major challenges for all of the microfabrication and nanofabrication technologies is to downscale the feature size while maintaining a high throughput. To increase the throughput and the ability to be used in production, the milling rate of the existing FIB milling systems has to be improved. A variable-diameter beam system should be developed to provide multi-resolution milling to cope with different accuracy or tolerance requirements. It is ideal that the beam diameter can be continuously changed *in situ*. This type of system has been available for many macroscale fabrication processes (Tseng 2001, Tseng and Tanaka 2001). With this system, a larger beam can be used for roughing ‘cut’ (milling) to increase the milling rate in regions where only lower resolution is needed. The advantages to use a heavy-duty two-lens system with improved automation should be examined with the goal to develop a system for limited production usage first. Once the high-performance FIB system is used in production, it can be a vital candidate to become the mainstream tool for the future microtechnology and nanotechnology industry.

Acknowledgments

The author gratefully acknowledges the support of this study by the US National Science Foundation under grant no DMI-0002466 and CMS-0115828. Special thanks go to Professor Andrew J Steckl of University of Cincinnati, Professor Michael J Vasile of Louisiana Tech University, Professor Andrei Stanishevsky of University of Alabama, Professor Lloyd R Harriott of University of Virginia, Professors Bryan K A Ngoi and Yongqi Fu of Nanyang Technology University, and Drs David P Pivin and George P Vakanas of Intel for their helpful discussions and providing useful information for this study. The assistance from Ivan Insua, Tom C Fan, Bharath Leeladharan, Martin Mitan, Bo Li and Jong S Park of Arizona State University in preparing this manuscript should be specifically acknowledged.

Appendix. Uniform ion intensity in milling

This appendix is to provide the mathematical formulation for obtaining a uniform ion distribution along and across

the scanning lines and for estimating the ion intensity of a FIB. A Gaussian profile is used to represent the ion intensity distribution of the beam. Mathematically, we can have (Weisstein 1999)

$$D(r, \sigma) = \frac{D_0}{\sigma \sqrt{2\pi}} \exp\left(-\left(\frac{r}{\sigma \sqrt{2}}\right)^2\right) \quad (\text{A1})$$

where D is the Gaussian distribution, D_0 is the dose constant, r is the radial coordinate and the beam center is located at $r = 0$. σ is the standard deviation of the Gaussian distribution, in which the beam diameter (d_f) equals 2.35σ (Weisstein 1999). Because the constant D_0 can be obtained by satisfying the condition in which the total input dose equals the total ions to the target within one dwell time, i.e., $\int \int D(r, \sigma) r dr d\theta = I_p t_d$, we can have

$$D_0 = (I_p t_d) / [(2\pi)^{1/2} \sigma] = 0.94 [I_p t_d / d_f] \quad (\text{A2})$$

where I_p is the beam current. If $D(r, \sigma)$ represents the ion density instead of the ion intensity, D_0 can also be found to be

$$D_0 = (I_p t_d) / [(2\pi)^{1/2} \sigma] = 0.94 [I_p t_d / (ned_f)], \quad (\text{A3})$$

where e is the electron charge and is equal to 1.60×10^{-19} C. n is the number of charge, in which $n = 1$ for a single-charged ion beam, while $n = 2$ for a double charged ion beam.

During milling, since the beam moves in a pixel-by-pixel motion and remains at each pixel for a time equal to the dwell time, t_d , the superimposed or overlaid ion intensity over the target substrate can be conveniently expressed by the Cartesian coordinates (x, y) as

$$D(x, y, \sigma) = \frac{D_0}{\sigma \sqrt{2\pi}} \sum_{m=0}^M \exp\left[-\left(\frac{x - m^x p_s}{\sigma \sqrt{2}}\right)^2\right] \times \sum_{n=0}^N \exp\left[-\left(\frac{y - n^y p_s}{\sigma \sqrt{2}}\right)^2\right] \quad (\text{A4})$$

where M is the total number of pixels involved in a specific scanning line, N is the total number of scanning lines considered, and x^p_s and y^p_s are the pixel spacings along and across the scanning lines, respectively. During milling, the beam center starts at $x = 0$ and $y = 0$ with movement following either raster or serpentine scan, i.e., along the scanning line (x -direction) or across the lines (y -direction). The normalized ion flux or intensity (\bar{D}) shown in figures 9–12 is defined as $\bar{D} = \sigma \sqrt{2\pi} D / D_0$.

References

- Adams D P, Vasile M J and Krishnan A S M 2000 Microgrooving and microthreading tools for fabricating curvilinear features *Precision Eng.* **24** 347–56
- Almen O and Burce G 1961 Collection and sputtering experiments with noble gas ions *Nucl. Instrum. Methods* **11** 257–78
- Ben Assayag G, Vieu C, Gierak J, Sudraud P and Corbin A 1993 New characterization method of ion current-density profile based on damage distribution of Ga^+ focused-ion beam implantation in GaAs *J. Vac. Sci. Technol. B* **11** 2420–6
- Bi J, de Jager P W H, Barth J E and Kruit P 1998 Influence of Coulomb interactions on current density distribution in a two-lens focused ion beam system *Microelectron. Eng.* **42** 249–52
- Biersack J P and Haggmark L G 1980 A Monte Carlo computer program for the transport of energetic ions in amorphous targets *Nucl. Instrum. Methods Phys. Res. B* **174** 257–69

- Bischoff L, Teichert J and Heera V 2001 Focused ion beam sputtering investigations on SiC *Appl. Surf. Sci.* **184** 372–6
- Blauner P G, Butt Y, Ro J S and Melngailis J 1989 Focused ion beam fabrication of submicron gold structures *J. Vac. Sci. Technol. B* **7** 609–17
- Brodie I and Muray J J 1992 Particle beams: sources, optics, and interactions *The Physics of Micro/Nano-Fabrication* (New York: Plenum) chapter 2
- Chyr I, Lee B, Chao L C and Steckl A J 1999 Damage generation and removal in the Ga⁺ focused ion beam micromachining of GaN for photonic applications *J. Vac. Sci. Technol. B* **17** 3063–7
- Davies S T and Khamsehpour B 1996 Focused ion beam machining and deposition for nanofabrication *Vacuum* **47** 455–62
- DeJager P W H and Vijgen L J 1994 Beam interactions in a focused ion-beam system with a liquid-metal ion-source *Microelectron. Eng.* **23** 107–10
- Edinger K and Kraus T 2000 Modeling of focused ion beam induced surface chemistry *J. Vac. Sci. Technol. B* **18** 3190–3
- Fabian J H, Scandella L, Fuhrmann H, Berger R, Mezzacasa T, Musil C, Gobrecht J and Meyer E 2000 Finite element calculations and fabrication of cantilever sensors for nanoscale detection *Ultramicroscopy* **82** 69–77
- Frey L, Lehrer C and Ryssel H 2003 Nanoscale effects in focused ion beam processing *Appl. Phys. A* **76** 1017–23
- Fu Y and Bryan N K A 2001 Experimental study of microcylindrical lenses fabricated using focused-ion-beam technology *J. Vac. Sci. Technol. B* **19** 1259–63
- Fu Y, Bryan N K A, San O A and Hong L B 2000a Data format transferring for fib microfabrication *Int. J. Adv. Manuf. Technol.* **16** 600–2
- Fu Y, Bryan N K A, Shing O N and Hung N P 2000b Influence of the redeposition effect for focused ion beam 3D micromachining in silicon *Int. J. Adv. Manuf. Technol.* **16** 877–80
- Fu Y, Bryan N K A, Shing O N and Wyan H N P 2000c Influence analysis of dwell time on focused ion beam micromachining in silicon *Sensors Actuators A* **79** 230–4
- Ganpule C S, Stanishevsky A Su, Aggarwal S Q, Melngailis J, Williams E and Ramesh R 1999 Scaling of ferroelectric properties in thin films *Appl. Phys. Lett.* **75** 409–11
- Harriott L R 1990 Beam-size measurements in focused ion beam systems *J. Vac. Sci. Technol. A* **8** 899–901
- Harriott L R 1991 Technology of finely focused ion beams *Nucl. Instrum. Methods Phys. Res. B* **55** 802–10
- Harriott L R and Vasile M J 1989 Focused ion beam secondary ion mass spectrometry: ion images and end point detection *J. Vac. Sci. Technol. B* **7** 181–7
- Hopkins L C, Griffith J E, Harriott L R and Vasile M J 1995 Polycrystalline tungsten and iridium probe tip preparation with a Ga⁺ focused ion beam *J. Vac. Sci. Technol. B* **13** 335–7
- Ishitani T, Ohnishi T, Madokoro Y and Kawanami Y 1991 Focused ion beam ‘cutter’ and ‘attacher’ for micromachining and device transplantation *J. Vac. Sci. Technol. B* **9** 2633–7
- Kaesmaier R and Loschner H 2000 Ion projection lithography: progress of European MEDEA & International Program *Microelectron. Eng.* **53** 37–45
- Latif A, Booij W E, Durrell J H and Blamire M G 2000 Real time resistometric depth monitoring in the focused ion beam *J. Vac. Sci. Technol. B* **18** 761–4
- Lehrer C, Frey L, Petersen S and Ryssel H 2001 Limitation of focused ion beam nanomachining *J. Vac. Sci. Technol. B* **19** 2533–8
- Li H W, Kang D J, Blamire M G and Huck W T S 2003 Focused ion beam fabrication of silicon print masters *Nanotechnology* **14** 220–3
- Lugstein A, Basnar B, Smoliner J and Bertagnoli E 2003 FIB processing of silicon in the nanoscale regime *Appl. Phys. A* **76** 545–8
- Madou M 1997 *Fundamentals of Microfabrication* (Boca Raton, FL: CRC Press)
- Melngailis J 1987 Focused ion beam technology and applications *J. Vac. Sci. Technol. B* **5** 469–95
- Melngailis J 2001 Applications of ion microbeams lithography and direct processing *Handbook of VLSI Lithography* 2nd edn ed J N Helbert (Park Ridge, NJ: Noyes) pp 791–855
- Melngailis J, Mondelli A A and Mohondro R 1998 A review of ion projection lithography *J. Vac. Sci. Technol. B* **16** 927–57
- Mitan M M and Pivin D P 2003 <http://www.eas.asu.edu/~fib/projects.htm> and www.eas.asu.edu/~fib/images/fiber01.jpg
- Nojima M, Tomiyasu B, Kanda Y, Owari M and Nihei Y 2002 Nanoscale SIMS analysis: the next generation in local analysis *Appl. Surf. Sci.* **203–204** 194–7
- Orloff J 1993 High-resolution focused ion beams *Rev. Sci. Instrum.* **64** 1105–30
- Pellerin J G, Shedd G M, Griffs D P and Russell P E 1989 Characterization of focused ion beam micromachined features *J. Vac. Sci. Technol. B* **7** 1810–2
- Picard Y N, Adams D P, Vasile M J and Ritchey M B 2003 Focused ion beam-shaped microtools for ultra-precision machining of cylindrical components *Precision Eng.* **27** 59–69
- Reyntjens S and Puers R 2001 A review of focused ion beam applications in microsystem technology *J. Micromech. Microeng.* **11** 287–300
- Ruchhoeft P, Colburn M, Choi B, Nounou N, Johnson S, Bailey T, Damle S, Stewart M, Ekerdt J, Sreenivasan S V, Wolfe J C and Willson C G 1999 Patterning curved surfaces: template generation by ion beam proximity lithography and relief transfer by step and flash imprint lithography *J. Vac. Sci. Technol. B* **17** 2965–9
- Santamore D, Edinger K, Orloff J and Melngailis J 1997 Focused ion beam sputter yield change as a function of scan speed *J. Vac. Sci. Technol. B* **15** 2346–9
- Stanishevsky A 1999 Focused ion beam patterning of diamond-like carbon films *Diamond Relat. Mater.* **8** 1246–50
- Steckl A J and Chyr I 1999 Focused ion beam micromilling of GaN and related substrate materials (sapphire, SiC, and Si) *J. Vac. Sci. Technol. B* **17** 362–5
- Takai M, Kishimoto T, Mimura R, Sawaraqi H and Aihara R 1996 Application of medium energy nuclear microprobe to semiconductor process steps *Nucl. Instrum. Methods Phys. Res. B* **118** 418–22
- Tseng A A 2001 Adaptable filament deposition system and method for freeform fabrication of three-dimensional objects *US Patent No. 6,251,340B1*
- Tseng A A, Chen K, Chen C D and Ma K J 2003 Electron beam lithography in nanoscale fabrication: recent development *IEEE Trans. Electron. Packag. Manuf.* **26** 141–9
- Tseng A A, Insua I A, Park J S, Li B and Vakanas G P 2004 Milling of submicron channels on gold film using double charged focused arsenic ion beam *J. Vac. Sci. Technol. B* **22** 882–9
- Tseng A A, Insua I A and Vakanas G P 2002 Maskless submicron machining by focused ion beams *Proc. 2002 NSF Design, Service and Manufacturing Grantees & Research Conf. (Arlington VA: US National Science Foundation)* pp 2043–4 MPM Paper
- Tseng A A and Tanaka M 2001 Advanced deposition techniques for freeforming metal and ceramic parts *Rapid Prototyping J.* **7** 6–17
- Tseng A A, Tang W C, Lee Y-C and Allen J 2000 *NSF 2000 Workshop on Manufacturing of Micro-Electro-Mechanical Systems J. Mater. Process. Manuf. Sci.* **8** 292–305
- Vasile M, Xie J and Nassar R 1999 Depth control of focused ion-beam milling from a numerical model of the sputter process *J. Vac. Sci. Technol. B* **17** 3085–90
- Wang L 1997 Design optimization for two lens focused ion beam columns *J. Vac. Sci. Technol. B* **15** 833–9
- Ward J W 1985 A Monte Carlo calculation of virtual source size for a liquid metal ion source *J. Vac. Sci. Technol. B* **3** 207–13
- Weisstein E W 1999 *Math World* (Boca Raton, FL: CRC Press) (<http://mathworld.wolfram.com/GaussianFunction.html>)

- Xiong G, Allwood D A, Cooke M D and Cowburn R P 2001 Magnetic nanoelements for magnetoelectronics made by focused-ion-beam milling *Appl. Phys. Lett.* **79** 3461–3
- Xu X, Ratta A D D, Sosonkina J and Melngailis J 1992 Focused ion beam induced eposition and ion milling as a function of angle of ion incidence *J. Vac. Sci. Technol. B* **10** 2675–80
- Yamaguchi H 1987 Line dose dependence of silicon and gallium arsenide removal by a focused gallium beam *J. Physique Coll. C6* (Supp. 11) pp C6.165–C6.170 Tome 48
- Yamaguchi A and Nishikawa T 1995 Low-damage specimen preparation technique for transmission electron microscopy using iodine gas-assisted focused ion beam milling *J. Vac. Sci. Technol. B* **13** 962–6
- Yamaguchi H, Saitoh K and Mizumura M 1998 End-point detection using focused ion beam-excited photoemissions in milling deep small holes in large scale integrated circuit structures *J. Vac. Sci. Technol. B* **16** 2555–61
- Yamaguchi H, Shimase A, Haraichi S and Miyauchi T 1985 Characteristics of silicon removal by fine focused gallium ion beam *J. Vac. Sci. Technol. B* **3** 71–4
- Yamamura Y, Itakawa Y and Itoh N 1983 Angular dependence of sputtering yields of monatomic solids *IIPJ-AM-26* (Nagoya University, Nagoya, Japan)
- Yongqi F and Bryan N K A 2000 Investigation of 3D microfabrication characteristics by focused ion beam technology in silicon *J. Mater. Process. Technol.* **104** 44–7
- Yongqi F and Ngai B K A 2000 Investigation of direct milling of micro-optical elements with continuous relief on a substrate by focused ion beam technology *Opt. Eng.* **39** 3008–13
- Young R J, Cleaver J R A and Ahmed H 1993 Characteristics of gas-assisted focused ion beam etching *J. Vac. Sci. Technol. B* **11** 234–41
- Yu X, Bi J and Lu J 1994 Single-lens focused ion beam system *Microfabrication Technol.* **3** 6–16 (in Chinese)